

RICE UNIVERSITY

**Exploration of Chemical Analysis Techniques for Nanoscale
Systems**

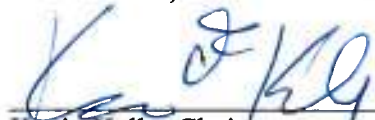
by

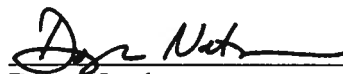
Albert Chang

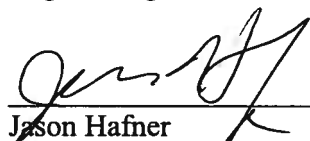
A THESIS SUBMITTED
IN PARTIAL FULFILLMENT OF THE
REQUIREMENTS FOR THE DEGREE

Doctor of Philosophy

APPROVED, THESIS COMMITTEE:



Kevin Kelly, Chair
Associate Professor in Electrical and
Computer Engineering

Doug Natelson
Professor of Physics and Astronomy
and Electrical and Computer
Engineering

Jason Hafner
Associate Professor of Physics and
Astronomy and Chemistry

Houston, Texas

October, 2012

Exploration of Chemical Analysis Techniques for Nanoscale Systems

Albert T. Chang

Abstract

As the critical dimensions of many devices, especially electronics, continue to become smaller, the ability to accurately analyze the properties at ever smaller scales becomes necessary. Optical techniques, such as confocal microscopy and various spectroscopies, have produced a wealth of information on larger length scales, above the diffraction limit. Scanning probe techniques, such as scanning tunneling microscopy and atomic force microscopy, provide information with an extremely fine resolution, often on the order of nanometers or angstroms. In this document, plasmon coupling is used to generate large signal increases, with clear future applications toward scanning probe optical spectroscopies. A variation on scanning tunneling microscopy is also used to study the surface structure of environmentally interesting nanoparticles. Traditional Raman spectroscopy is used to examine doped graphene, which is becoming a hot material for future electronic applications.

Acknowledgements

First and foremost I would like to thank my family for their continued support through my time performing this research. My advisor, Dr. Kevin Kelly, also deserves a lot of thanks as well for sticking with me through thick and thin. I would like to thank my committee as well for bearing with some of my various issues. All former and current members of the Kelly lab, particularly Dr. Rajiv Giridharagopal and Corey Slavonic, at Rice University have also been very helpful in providing useful discussion. Dr. Roman Gomez, Dr. Gary Kilper, Dr. Aaron Coyner, Mike Mott, and Greg Brunner also contributed greatly to helping me maintain my overall sanity as well as keeping the axe on the grinder, so to speak.

Table of Contents

Abstract	ii
Acknowledgements	iii
List of Figures	vi
1. Outline	1
2. Plasmon Coupling between a Gold Colloid and Thin Gold Film	3
2.1 Raman Spectroscopy.....	3
2.2 Raman Scattering Theory.....	4
2.3 Surface Enhanced Raman Spectroscopy.....	8
2.4 Motivation.....	13
2.5 Instrumentation.....	14
2.6 Experimental Details.....	16
2.7 Experimental Results.....	19
2.7.1 PVP Spacer, PMA Analyte.....	21
2.7.2 PMA Spacer and Analyte.....	24
2.8 Discussion.....	37
3. Work Function STM of palladium coated gold nanoparticles	29
3.1 Scanning Tunneling Microscopy.....	29
3.2 Basic STM Theory.....	30
3.3 dI/dZ Spectroscopy.....	31
3.4 Self-Assembled Monolayers.....	33
3.5 Motivation.....	36
3.6 Experimental Setup.....	38
3.7 Experimental Results.....	39
3.8 Discussion and Conclusions.....	44
4. Raman Imaging of Nitrogen Doped Graphene	46
4.1 Graphene.....	46
4.2 Graphene Basics.....	47
4.3 Graphene Raman.....	48
4.4 Doped Graphene.....	51
4.5 Motivation.....	52
4.6 Experimental Setup.....	53
4.7 Experimental Results.....	54

4.8 Discussion and Conclusions.....	63
5. Conclusions and Future Work	65
5.1 Nanoparticles over Thin Film.....	65
5.2 Work Function of Nanoparticles in STM.....	67
5.3 Raman Spectroscopy of Graphene.....	69
References	72

List of Figures

Figure 2.1. Stokes (left) and Anti-Stokes (right) Raman Scattering Diagrams

Figure 2.2. Calculations performed on the gold colloid over gold film geometry, 4 nm film and 4 nm separation (left), 4 nm film and 8 nm separation (middle), 8 nm film and 4 nm separation (right) [28]

Figure 2.3. Beam Path for Colloid on Film Experiments

Figure 2.4. AFM and Cross Sections of gold films prepared using base bath cleaned and rinsed glass slides. Top Left: AFM image of 20 nm gold film on base bath cleaned glass. Top Right: Typical cross section of the film on base bath cleaned glass. Bottom Left: AFM image of 20 nm gold film on rinsed glass slide. Bottom Right: Typical cross section of the film on rinsed glass

Figure 2.5. Chemical Structure of para-mercaptoaniline; blue represents nitrogen, cyan represents sulfur, black represents carbon, and gray represents hydrogen

Figure 2.6. Two AFM images (left) and confocal image (right) illustrating correlation, boxes added to show correlation, the bottom box corresponds to the bottom AFM image and the top box corresponds to the top AFM image

Figure 2.7. AFM (left) and Confocal Raman (right) images of 50 nm colloid on 20 nm film with poly-4-vinylpyridine spacer

Figure 2.8. AFM (left) and Raman (right) images of 80 nm colloid over 20 nm film with poly-4-vinylpyridine spacer, shapes added to illustrate correlation.

Figure 2.9. AFM image of para-mercaptoaniline on a 20 nm gold film

Figure 2.10. SEM (Top and Bottom Left), AFM (Top and Bottom Middle) and Raman (Top and Bottom Right), of 80 nm nanoparticles on 20 nm gold film with no poly-4-vinylpyridine spacer.

Figure 2.11. Matlab cross-sections of the sphere (top row), and disk (bottom row), performed on the SEM (left column) and AFM (right column) images.

Figure 3.1. Basic dI/dZ STM setup

Figure 3.2. Side-view schematic of an alkanethiolate SAM on Au. Purple represents gold, yellow sulfur, black the carbon backbone of the alkanethiol, and white hydrogen.

Figure 3.3. Left: STM of hexanethiolate SAM on gold, center: STM of decanethiolate SAM on gold, right: STM of decanethiolate SAM on gold showing lower concentration domains

Figure 3.4. Schematic of the entanglement process between a nanoparticle and a SAM

Figure 3.5. Topography (left) and work function (right) images of Au nanoparticles entangled onto a decanethiolate SAM.

Figure 3.6. Topography (left) and work function (right) images of Pd nanoparticles entangled onto a decanethiolate SAM

Figure 3.7. Topography (left) and work function (right) images of AuPd nanoparticles entangled onto a decanethiolate SAM.

Figure 4.1. Pattern of carbon atoms in graphene

Figure 4.2. Energy level diagram of the origin of the $2D$ peak. The incoming laser excites an electron hole pair (blue). The first electron-phonon scattering event occurs (brown). The electron is scattered back by the same phonon (green). The electron relaxes back to the ground state, emitting the $2D$ peak photon (red).

Figure 4.3. Energy level diagram of the origin of the D peak. The incoming laser excites an electron hole pair (blue). The first electron-phonon scattering event occurs (brown). The electron is scattered by a defect (green). The electron relaxes back to the ground state, emitting the D peak photon (red).

Figure 4.4. G peak (top), $2D$ peak (middle) and $2D/G$ ratio (bottom) for undoped graphene on ITO

Figure 4.5. Optical (left) and $10 \times 10 \mu\text{m}$ AFM (middle) of a selected region of an undoped graphene sample and a $5 \times 5 \mu\text{m}$ confocal microscopy (right) centered on the cross overlayed on the AFM image

Figure 4.6. D peak (upper left), G peak (upper right), and $2D$ peak (bottom) Raman images, diamond, square, and circle denote locations where individual spectra were extracted and analyzed.

Figure 4.7. Spectra from the labeled locations in Figure 4.6

Figure 4.8. Typical spectrum of undoped graphene on ITO

Figure 4.9. Typical spectrum of N-doped graphene on ITO

Figure 4.10. G peak (left), $2D$ peak (right) and “N” peak images (bottom) of an N-doped graphene sample

Figure 4.11. G peak shift from $1591 \text{ rel. } 1/\text{cm}$ (left) and “N” peak image (right). Red circle denotes area of high nitrogen concentration while the blue circle denotes an area of lower concentration.

Chapter 1

Outline

Nanoscale chemical analysis is a field of great interest. As electronics continue to shrink in size, the ability to accurately characterize devices at the nanoscale grows in importance. A variety of techniques exist for examining samples of interest, and this document will display the utility of these experimental methods and provide a route for the expansion of each technique's capabilities.

Chapter 2 describes the various techniques used throughout the document. The primary scientific principles and instrumentation used involve Raman spectroscopy and scanning tunneling microscopy. Surface enhancement of Raman scattering and graphene are also described, as they both play a crucial role in the experimental chapters to follow. Surface enhanced Raman scattering potentially provides a unique bridge between the optical and scanning probe regimes and is examined further in Chapter 3. Graphene is a particularly interesting material of interest and is probed in Chapter 5.

In Chapter 3, the use of plasmonic engineering to allow for the potential expansion of surface enhanced Raman scattering into the nanoscale realm is investigated. The coupled plasmon between a nanoparticle and a film is used to enhance the signal of the analyte molecule. Atomic force microscopy and scanning electron microscopy are both used to confirm that the signal results from just a single particle, as coupled particles are known to generate large enhancements as well.

The use of an established scanning probe technique, scanning tunneling microscopy, to obtain some chemical information from specialized nanoparticles is covered in Chapter 4. While scanning tunneling microscopy typically only provides

electrical and topographical information, some minor modifications make extraction of some chemical information possible, for instance dI/dZ spectroscopy. Through the use of this technique, the surface structure of these nanoparticles is reinforced.

Chapter 5 details the work done with conventional Raman spectroscopy to explore doping in graphene. Because graphene is gaining a lot of interest for electronic applications, the ability to analyze dopant levels in graphene is becoming important. This Chapter will show the power of Raman spectroscopy in determining these dopant profiles.

The final chapter, Chapter 6, will provide detailed discussion of conclusions and what future experiments can be performed to improve upon the results presented in the rest of the document.

Chapter 2

Plasmon Coupling Between a Gold Colloid and Thin Gold Film

2.1 Raman Spectroscopy

First discovered in 1928 by Sir Chandrasekhara Venkata Raman, this type of vibrational spectroscopy was somewhat limited in its earlier years by the lack of radiation intense enough to generate a strong enough optical signature from samples being studied [1]. With the advent of lasers, however, Raman spectroscopy attained a much higher level of usefulness. Lasers provided a sufficiently powerful source of a single wavelength, making it possible to accurately obtain and interpret Raman scattered spectra. Lasers also made it possible to create additional techniques based on similar principles, such as Coherent Anti-Stokes Raman Scattering [1]. Since then, a variety of molecules and materials have been studied with this powerful chemical probe, including superconductors, semiconductors, biological materials, polymers, and many other materials of scientific interest [2]. Until the 1970s, however, studies were mostly limited to bulk systems and materials with a large Raman scattering cross section, because even with the arrival of the laser, the Raman scattering cross section, in general, was still small enough to pose problems for more general usage. In the 1970s, the surface enhancement of the signal was discovered by van Duyne [3], through which even sub-monolayer amounts of molecules deposited onto certain metallic surfaces could generate a detectable Raman signal. The discovery of surface enhancement opened up a new world of samples that could be analyzed, a world where the sensitivity of Raman spectroscopy is much greater and the potential for analyzing almost any system of interest is opened. The progress made studying the mechanisms controlling the surface enhancement of Raman

scattering as well as the engineering of substrates to optimize this effect have even lead to the possibility of optical information at the nanoscale and realization Raman spectroscopy beyond the far-field diffraction limit, see for instance the work performed by Novotny, et. al., on carbon nanotubes [4-5]. This powerful analysis technique holds much promise for further bridging the gap between optical and scanning probe microscopies, and as a result has garnered much interest.

2.2 Raman Scattering Theory

Raman scattering, at a very basic level, is an inelastic scattering phenomenon by which a photon loses, or more rarely gains energy, by interacting with vibrational modes of the object it is scattered from. That is to say, an incoming photon with initial energy $\hbar\omega_i$, collides with some molecule at an initial energy E_i , and after the collision, the same photon leaves with a final energy $\hbar\omega_f$ while the molecule has its energy changed to E_f [1]. A schematic detailing this process is shown in Figure 2.1 below.

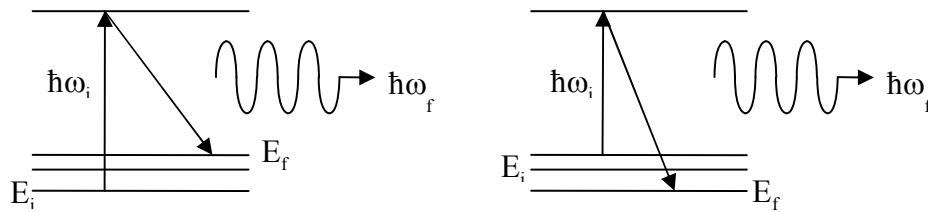


Figure 2.1: Stokes (left) and Anti-Stokes (right) Raman Scattering Diagrams

While this process generally occurs with the photon losing energy and the molecule gaining energy ($\hbar\omega_f < \hbar\omega_i$ and $E_i > E_f$), this is not always the case. In the

case of Stokes scattering, the photon loses energy to the molecule during the scattering process. When anti-Stokes scattering occurs, if the photon scatters off of a molecule that is already in an excited state, the photon actually gains energy from the molecule during the scattering. Therefore, in the case of Stokes scattering, the transfer of energy goes as [1]:

$$\hbar\omega_i + M(E_i) \rightarrow \hbar\omega_f + M(E_f) \text{ where } \hbar(\omega_i - \omega_f) = E_f - E_i > 0$$

And naturally, in the case of anti-Stokes scattering, the inequality switches such that:

$$\hbar(\omega_f - \omega_i) = E_i - E_f > 0$$

It is important to note that the excited energy level reached after the photon and molecule initiate scattering does not have to be an actual eigenstate of the molecule, rather, it is merely a virtual state formed by the photon-molecule system [1]. In the case where this virtual level coincides with a real state of the molecule, however, resonance Raman scattering occurs [1] and there can be some enhancement of the Raman signal from that effect, although this enhancement is much smaller than one typically sees from surface enhanced Raman spectroscopy, which will be expanded upon in a later section.

A classical description of vibrational Raman scattering [1] starts from the equation:

$$\rho = \mu_0 + \tilde{\alpha}E$$

where ρ is the dipole moment of the molecule, μ_0 represents any permanent dipole moment, and $E = E_0 \cos \omega t$ is the incident wave. The $\tilde{\alpha} E$ is the induced dipole moment, where the quantity $\tilde{\alpha}$ is the polarizability tensor, generally of rank two [1]. If we assume that the system is off resonance, Taylor expand the dipole moment and polarizability in

the normal coordinates of the nuclear displacements, and also assume small vibrational amplitudes, we obtain, for the total dipole moment [1]:

$$\begin{aligned} \rho = & \mu_0 + \sum_{n=1}^Q \left(\frac{\partial \mu}{\partial q_n} \right)_0 q_{n0} \cos(\omega_n t) + \alpha_{ij}(0) E_0 \cos(\omega t) \\ & + \left(\frac{1}{2} \right) E_0 \sum_{n=1}^Q \left(\frac{\partial \alpha_{ij}}{\partial q_n} \right)_0 q_{n0} [\cos(\omega + \omega_n)t + \cos(\omega - \omega_n)t] \end{aligned}$$

Where $Q = 3N-6$ for the number of vibrational modes for N nuclei, $\alpha_{ij}(0)$ is the polarizability at equilibrium, which is the $q_n = 0$ state. From this derivation four distinct terms appear. The first term, μ_0 , is any permanent dipole moment, as stated above. The second term,

$$\sum_{n=1}^Q \left(\frac{\partial \mu}{\partial q_n} \right)_0 q_{n0} \cos(\omega_n t)$$

describes the infrared spectrum, the third term,

$$\alpha_{ij}(0) E_0 \cos(\omega t)$$

represents the Rayleigh scattered, or elastically scattered, light, and the fourth term,

$$\left(\frac{1}{2} \right) E_0 \sum_{n=1}^Q \left(\frac{\partial \alpha_{ij}}{\partial q_n} \right)_0 q_{n0} [\cos(\omega + \omega_n)t + \cos(\omega - \omega_n)t]$$

describes the Raman scattered light, where $(\omega + \omega_n)$ and $(\omega - \omega_n)$ terms represent the anti-Stokes and Stokes scattered light, respectively. Although this classical description is useful for predicting the spectral location of the Raman peaks, one must incorporate quantum mechanics to predict relative intensities of these peaks.

When quantum mechanics is incorporated, the expectation value of the polarizability tensor, after approximating the molecular potential by a harmonic potential,

neglecting coupling between vibrational modes, and using an orthogonality relation [1], is given by:

$$\langle \alpha_{ij} \rangle_{ab} = (\alpha_{ij})_0 + \sum_{n=1}^Q \left(\frac{\partial \alpha_{ij}}{\partial q_n} \right)_0 \int w_n(q_n, v_a) q_n w_n(q_n, v_b) dq_n$$

where the first term leads to Rayleigh scattering, and from the second term falls out the basic intensity parameter of Raman spectroscopy, which is the derivative term within the summation [1]. For a more detailed look at the intensity expected at each Raman peak, one must use the relation [1]:

$$I_s = N_i(E_i) \sigma_R(i \longrightarrow f) I_L$$

which states that the intensity of the particular line, I_s , is equal to the product of the population density of the initial molecular state, $N_i(E_i)$, the scattering cross section, $\sigma_R(i \longrightarrow f)$, and the intensity of the incoming laser light, I_L . From the matrix elements of the polarizability tensor, the following relation for the scattering cross section falls out:

$$\sigma_R(i \longrightarrow f) = \left(\frac{8\pi\omega_s^4}{9\hbar c^4} \right) \left(\sum_J \left(\frac{\langle \alpha_{ij} \rangle \hat{e}_L \langle \alpha_{jf} \rangle \hat{e}_s}{\omega_{ij} - \omega_L - i\gamma_j} + \frac{\langle \alpha_{ji} \rangle \hat{e}_L \langle \alpha_{ff} \rangle \hat{e}_s}{\omega_{ff} - \omega_L - i\gamma_j} \right) \right)^2$$

From this relation, it becomes clear that vibrational modes not accessible by infrared spectroscopy are accessible by Raman spectroscopy. Also, although exact calculation of the scattering cross section can be difficult because of the need to know the molecular wave functions, the resonance Raman effect - where the Raman signal is enhanced by exciting with an energy that matches a molecular level transition - is clearly evident from the equation above. Although this source of enhancement can be significant, we are more interested in the phenomenon of SERS, where enhancements can reach enormous proportions.

2.3 Surface Enhanced Raman Spectroscopy

SERS was first discovered by van Duyne in the 1970s using systems of organic molecules coating silver nanoparticles [3]. Studying this system, he found that the metal surface enhanced the Raman signal by a factor on the order of 10^6 , spawning a new avenue of research for this powerful chemical analysis tool. SERS generally involves a metal, because the plasmon resonances inherent in metals tend to enhance the signal. Copper, gold, and silver are among the most commonly used metals when fabricating particles or surfaces for SERS usage, although there is interest in many other metals, for instance platinum and aluminum [3]. This enhancement can arise from two mechanisms, the electromagnetic and the chemical. The chemical enhancement factor involves enhancing the polarizability of the molecule due to interactions with the surface, for instance via a charge-transfer mechanism. The electromagnetic mechanism, which is more pertinent to these studies, relies on exciting the plasmon resonance of the surface on which the molecules have been placed.

A plasmon is a collective oscillation of an electron cloud. In the systems of interest, this represents the electron cloud of a metal particle or surface oscillating in a coherent fashion. As would be expected, the geometry and composition of the surface, and the resultant geometry of the electron cloud, play a crucial role in determining at what frequency the collective oscillation will occur. That is to say, the shape of the particle or surface, as well as the metal itself, determine where the wavelengths where the plasmon resonances are most pronounced. While for a bulk metal the plasmon frequency is merely the plasma frequency, the situation changes markedly when changing the

structure from a bulk slab of metal to various nanoparticle geometries, or even moving from a bulk metal to a thin film of the same metal [6]. More specifically, the bulk plasmon frequency of a particular metal in air is equal to its plasma frequency, ω_p . If we take the same metal, but instead make a thin film, the plasmon frequency changes roughly to $\omega_p/\sqrt{2}$, and if we make a small spherical particle instead of a thin film, the plasmon resonance roughly changes to $\omega_p/\sqrt{3}$ [6]. To distinguish between the plasmons of a bulk metal and the plasmons of nanostructures, the bulk material's plasmon is often referred to as a bulk plasmon while the nanostructure plasmons are typically called surface plasmons. This difference in terminology is not purely cosmetic, as bulk plasmon modes are not restricted by any boundary conditions while surface plasmons, by the very nature of the geometries they arise from, must conform to the boundaries with which they are restricted.

The plasmon resonances of many nanoparticle and surface geometries have been previously studied. To illustrate just how shape can change the plasmon resonance of a nanoparticle, three nanoparticles that have received a fair amount of study, namely gold colloid, gold nanorods, and gold nanoshells, will be discussed in detail. Gold colloid, as the name suggests, are simply nanospheres of gold, with sizes on the order of tens of nanometers. As described above, we would expect the plasmon of these particles to lie at around $\omega_p/\sqrt{3}$. This simplified expression assumes that the dielectric constant of the material stays exactly the same with the size of the particle. In actuality, the plasmon frequency depends on the size of the particle, because the condition used to find the plasmon frequency, namely the frequency at which $\epsilon = -2\epsilon_m$, becomes the frequency at which $\epsilon = -(2 + \frac{12}{5}x^2)\epsilon_m$, where x is the size of the particle and ϵ_m is the dielectric

constant of the embedding medium, after retaining more terms in the series expansions used to obtain this condition. For gold colloid, this translates to a plasmon frequency ranging from about 500 nm to 600 nm, with the plasmon frequency increasing with increasing particle size [7]. While this has proven useful, other geometries, such as nanorods and nanoshells, show more wide-scale applicability.

Gold nanorods, or nanoscale cylinders of gold, show two distinct, and tunable, plasmon resonances [8-10]. This phenomenon arises out of the fact that there are two plasmon modes that can exist with a particle of this geometry - the transverse and longitudinal plasmon modes. The longitudinal mode corresponds to the plasmon along the length of the cylinder, while the transverse mode is perpendicular to the longitudinal mode and runs along the width of the cylinder. The location of the transverse mode absorption peak lies in a similar range to that found for gold colloid, while the longitudinal peak occurs in the long wavelength visible or near infrared range, depending on the aspect ratio of the particular nanorod [9]. Nanorods show promise for SERS applications because the tunability of the longitudinal plasmon allows for engineering substrates to exhibit SERS at a specific desired wavelength. While nanorods are desirable because of their tunability and polarization-specific interaction with incident radiation, a property that arises from the fact that nanorods are not spherically symmetric, another family of nanoparticles, the nanoshell, exhibits a much wider range of tunability.

Nanoshells consist of a spherical dielectric core, usually composed of, but not limited to, silica, coated with a metal shell, in this case gold. The plasmon resonance of these particles depends on the core-shell thickness ratio, and are widely tunable, ranging from the visible to fairly deep into the infrared [11-13]. Increasing the thickness of the

shell produces a plasmon peak that is further toward the blue end of the spectrum, and approaches the limit of a gold colloid plasmon peak at the extreme [13]. Toward the other limit, that of an extremely small metallic shell around the dielectric core, the peak can shift out to the one micron range or even longer [13]. This tunability arises because the system can be modeled as two distinct plasmons, a sphere plasmon and a cavity plasmon, interacting with each other to produce the overall system plasmon. The thickness of the shell relative to the core, in this model, controls the degree to which these two plasmons interact with each other, and thus controls exactly where the peak will lie. Nanoshells are an extremely attractive plasmonic particle option, precisely because of this very wide range of tunability.

The plasmon resonances of the surface are the main reason for the electromagnetic enhancement mechanism behind SERS. This arises because the excitation of the plasmon also generates a large increase in the local electric field, and since the enhancement factor can be simply expressed as:

$$E = |E(\omega)|^2 |E(\omega')|^2$$

where E is the enhancement factor, $E(\omega)$ is the local electric field enhancement at the incident frequency, and $E(\omega')$ is the field enhancement at the Stokes shifted frequency [3]. This often leads to an enhancement on the order of E^4 since the width of the plasmon peak is generally greater than the Stokes shift, although one must be careful when calculating exact enhancement factors since this is not always the case [3]. Another factor to be aware of is the fact that the maximum electric field enhancement is not generally evenly distributed about the entire surface of the nanoparticle and depends strongly on nanoparticle or surface geometry and the polarization of the incident radiation.

Therefore, when calculating expected enhancements, one must take into account the location of the enhancement and the expected incident polarization. In light of these factors, however, the desirability of controllably tunable plasmonic substrates becomes clear. Since attempting to control the wavelength of the incident radiation can be a prohibitively expensive process, having the ability to tailor a substrate to the available lasers at hand becomes an extremely useful tool. Also, being able to control geometries such that the sample of interest lies within the region of maximum enhancement is also a key to tailoring plasmonic substrates to better fulfill SERS demands.

A variety of substrates have been used in SERS applications. Roughened gold and silver films [14-17] rely on generating the appropriate plasmon resonance through somewhat arbitrary chance, given that random roughening will likely produce some “hot spots,” regions of large field enhancement, are likely to appear. Gold and silver colloid, described above, have also been used with some success in SERS applications [18-20], where they utilize the well characterized colloid resonance or the junction plasmon resonance. This plasmon resonance arises from the coupling of nearby spherical plasmons. Alternatively, substrates fabricated using nanoscale lithography, such as the process which generates triangular gold islands on a surface by first evaporating through a monolayer of polystyrene spheres and then removing the spheres, has also found some success in this field [21-23]. Gold nanoshells, also described above, have also had great success in SERS applications [24-26]. Many other substrate architectures have found use as well [2], showing that this is a rich field that requires more research and attention.

2.4 Motivation

As has been mentioned before, Raman information at a nanoscale level would represent a huge leap forward in the imaging and nanoscale chemical analysis of various samples. Other scanning probe techniques, such as AFM and STM, provide topographic or electronic information. Standard optical microscopy, even with a confocal setup, only provides information with a resolution of a few hundred nanometers, depending on the incident wavelength used. Even standard NSOM techniques, which provide optical information with roughly the desired resolution, only provide limited optical information without any enhancement of the resulting signal. While NSOM, and especially apertureless NSOM, shows great promise in obtaining detailed optical information on the nanoscale, specifically from Raman scattering, some modifications and improvements must be made before this is a widespread reality.

Many efforts towards realizing the collection of detailed optical information at the nanoscale have taken place. Precise plasmonic engineering would provide a great deal of progress toward realizing the goal of nanoscale chemical information collection, but thus far this area has somewhat lagged behind. To this end, a better understanding of tip plasmons, as well as the interaction between tip and sample surface plasmons, would greatly enhance the understanding and ability to engineer such near field probes.

To enhance the understanding of the interplay between near field tip and surface plasmons, we have performed a collection of experiments on gold colloid over thin gold film samples. This architecture has shown a great deal of theoretical promise, and experimental promise in the macroscopic regime, in having the ability to greatly enhance signals at incident wavelengths of Raman interest, mainly in the infrared range to avoid

exciting the fluorescence of any samples being studied [27-28]. This enhancement, which occurs at a lower energy than the isolated colloid plasmon, is also expected to remain localized to the junction between the colloid and thin gold film, as is shown in Figure 2.2 [28]. While bulk measurements of similar systems have been performed [29-30], signal from nanoparticles over thin gold films correlated with AFM images to demonstrate that the signal comes from single particles have not yet been observed. We have performed confocal Raman studies on this gold colloid over thin gold film samples in the hopes of better understanding the system for future incorporation into NSOM Raman imaging instrumentation.

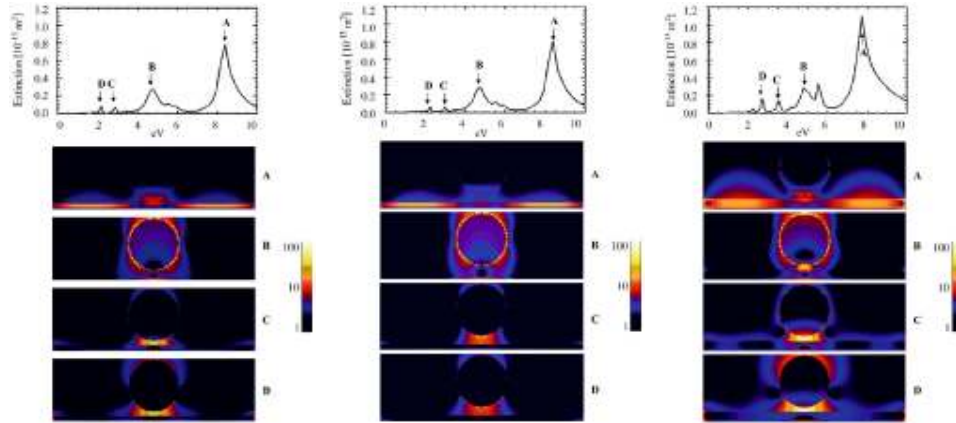


Figure 2.2: Calculations performed on the gold colloid over gold film geometry, 4 nm film and 4 nm separation (left), 4 nm film and 8 nm separation (middle), 8 nm film and 4 nm separation (right) [28]

2.5 Instrumentation

All experiments were performed on a commercial WiTec NSOM system. This system is desirable because of its supreme flexibility, as it incorporates confocal microscopy, AFM, and NSOM capabilities. Because of its flexibility, it is quite easy to perform an AFM analysis of the sample and then probe the same area with a confocal

setup to obtain closely correlated optical information of the same area. The laser used was a commercially available 785 nm near infrared laser, which would avoid exciting any native colloid plasmon resonance, because gold colloid has a plasmon resonance between 500 nm and 600 nm, therefore any signal produced can be attributed to either colloid-colloid junction hot spots or colloid-film interactions. The laser is focused on the sample and the back reflected signal is collected using a 100 times, 0.9 NA objective available from Nikon. The signal is then coupled into a fiber and sent to a spectrometer purchased with the system from Andor. The sample is raster scanned by moving the sample base and using piezoelectric components. The beam path is shown in Figure 2.3 below. At first glance it would appear that the direction of the incoming laser beam would serve to be a problem, since the laser is perpendicular with respect to the sample, leading to an electric field that is polarized in some way in the plane of the sample. To properly excite the junction plasmon, some component of the electric field must be oriented perpendicularly to the sample as well. This problem is somewhat alleviated by the fact that tightly focused Gaussian beams, because of the tight focusing, can generate some component of the electric field in the proper direction [4]. Although this is still not ideal, and could be improved with an annular illumination system [31], and although the signal is expected to be weaker than would be expected with a laser incident from the side at some angle, it is still strong enough to give us a signal off of the sample being studied.

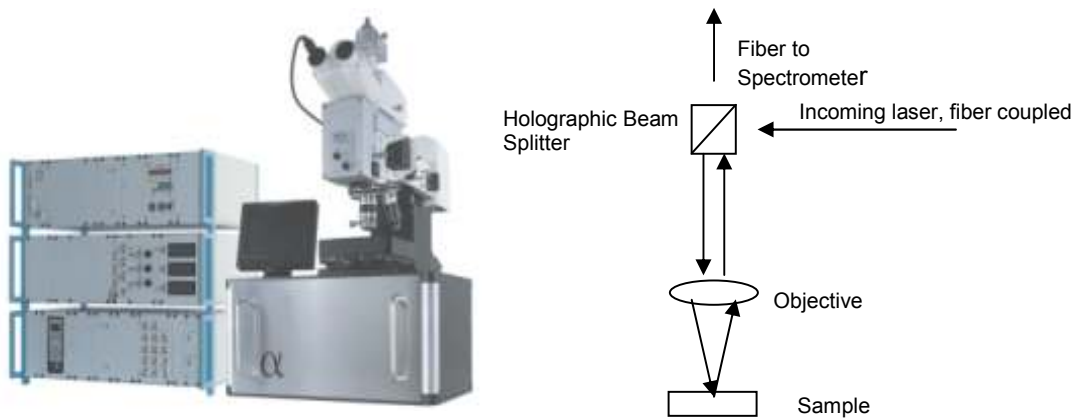


Figure 2.3: Beam Path for Colloid on Film Experiments

2.6 Experimental Details

As described above, all of the samples analyzed involve deposition of gold colloid over a thin gold film, with a small dielectric spacer layer to prevent actual contact between the surface and the colloid, because the region where the greatest enhancement is expected is the space between the colloid and the surface. The gold films were prepared by e-beam evaporation in a Sharon e-beam evaporator after cleaning the glass slides by either soaking in base bath or rinsing in ethanol. As shown in Figure 2.4, both of these methods seem to generate gold films that are smooth enough for use.

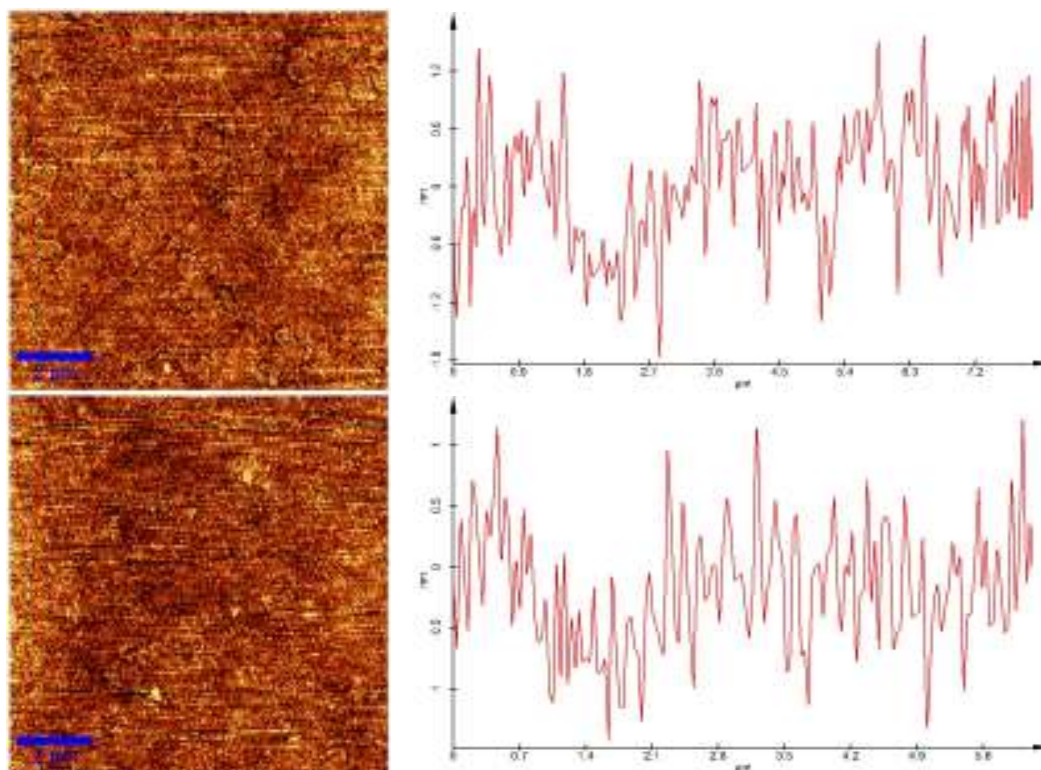


Figure 2.4: AFM and Cross Sections of gold films prepared using base bath cleaned and rinsed glass slides. Top Left: AFM image of 20 nm gold film on base bath cleaned glass. Top Right: Typical cross section of the film on base bath cleaned glass. Bottom Left: AFM image of 20 nm gold film on rinsed glass slide. Bottom Right: Typical cross section of the film on rinsed glass

Both films show a roughness of between about -1 and 1 nm, up to a maximum of 2 nm, and while a smaller roughness would be ideal, this small of a variation should not interfere with the study of these samples. After ascertaining that the films were smooth enough, they were deposited into a 100 μm solution of para-mercaptoaniline for at least 30 minutes to build a self assembled monolayer of this molecule on the surface of the gold film, to serve both as the analyte being studied as well as the dielectric spacer layer between the nanoparticles and the gold film. Early experiments, indicated in the results

section, dipped into a 1% by weight solution of poly-4-vinylpyridine in ethanol, before adding para-mercaptoaniline, to serve as the spacer layer.

Poly-4-vinylpyridine has been shown to be a useful polymer in immobilizing colloid on any surface [32]. Although the thickness of this layer is somewhat unknown, it has been previously reported that it forms a layer of about 5 nm thick [27].

Para-mercaptoaniline is a well studied, Raman active molecule [12, 13, 24]. Its structure is shown in Figure 2.5 below. It is a convenient analyte to use the mercapto group is known to self assemble onto gold, and the amine group is known to have an affinity for gold, which aids in the immobilization and binding of gold nanoparticles onto the samples. In addition, because it has been studied extensively, the Raman peaks for this molecule are known to occur at 1,590; 1,180; 1,077; 1,003; and 390 relative inverse cm. The conjugated ring core is also known to produce a larger than normal Raman scattering cross section. These factors led to para-mercaptoaniline being a natural choice for these experiments.

After the self-assembled monolayer was formed, a solution of dilute nanoshells and spherical gold nanoparticles of the desired size was drop cast onto the surface. The nanoshells serve as convenient markers for preliminary aligning of AFM and confocal microscopy images, and so were added in a very dilute concentration to ease the task of locating the same area for optical study after scanning with an AFM. After allowing this solution to dry overnight, it was then rinsed to remove as much excess nanoshells, colloid, or para-mercaptoaniline, as possible and then studied in the instrument.

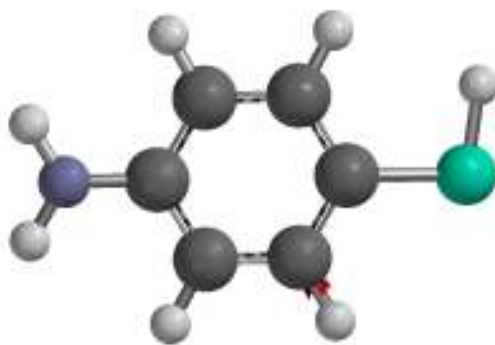


Figure 2.5: Chemical Structure of para-mercaptoaniline; blue represents nitrogen, cyan represents sulfur, black represents carbon, and gray represents hydrogen

All of the nanoshells used in this experiment were prepared by the Halas group at Rice University and all of the gold colloid used was purchased from Ted Pella. The gold shot used to prepare the gold films in the e-beam evaporator were purchased from Kamis and are guaranteed to have 99.999% purity. The para-mercaptoaniline is obtained in a solid form from Sigma-Aldrich.

2.7 Experimental Results

The samples were aligned with the confocal setup by first obtaining a regular confocal microscopy image, by which the nanoshells could be seen and alignment is possible. An example of this is shown in Figure 2.6, where a series of AFM images and a confocal image are shown to illustrate how this is made possible.

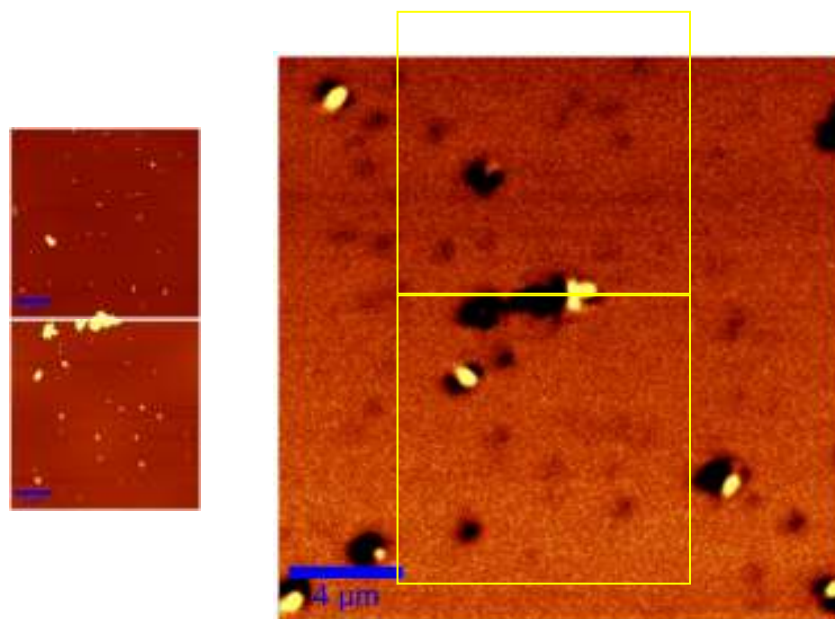


Figure 2.6: Two AFM images (left) and confocal image (right) illustrating correlation, boxes added to show correlation, the bottom box corresponds to the bottom AFM image and the top box corresponds to the top AFM image

In the figure above, each of the AFM images is a 10 by 10 micron square and the confocal image is a 30 by 30 micron image. The nanoshells clearly aid in alignment, as one can observe the large clump of nanoshells in the middle of the confocal image and line it up with the large clump seen in the AFM images, in this case between the top and middle image. After checking a few more landmarks, this clearly lines up properly. In the confocal image, especially near clumps of nanoshells, regions of high reflectivity appear. This is most likely due to the junction plasmon of the nanoshells increasing the scattering of the incoming laser radiation, thus increasing the signal reflected off of the

surface. There are also a series of slightly dark regions that do not match with any nanoshells in the AFM scan. These regions, however, do correlate strongly with aggregates of gold colloid, probably due to the fact that the junction plasmon of these colloids is causing additional absorption of the incoming laser. This phenomenon is somewhat interesting, but it does not affect our ability to align areas in this manner. Using a combination of nanoshells and confocal microscopy, it is possible to easily and repeatably ensure that the same area probed by AFM is indeed being probed by the confocal Raman scans which will be discussed below.

2.7.1 PVP Spacer, PMA analyte

When analyzing the 50 nm colloid on 20 nm film sample, there appears to be little, if any, enhancement from the coupling of the colloid and film plasmons. In Figure 2.7, while the nanoshells exhibit strong Raman scattering in the confocal Raman scans, all of the colloid in the area show no para-mercaptoaniline Raman signature. The integration time used was three seconds per pixel, so if enhancement were indeed occurring we would expect to see some trace of this. While the exact laser power has not been quantified, as will be made clear in a later section, it is more than sufficient to generate Raman scattering from this sort of system on these time scales if enhancement of the Raman signal were occurring.

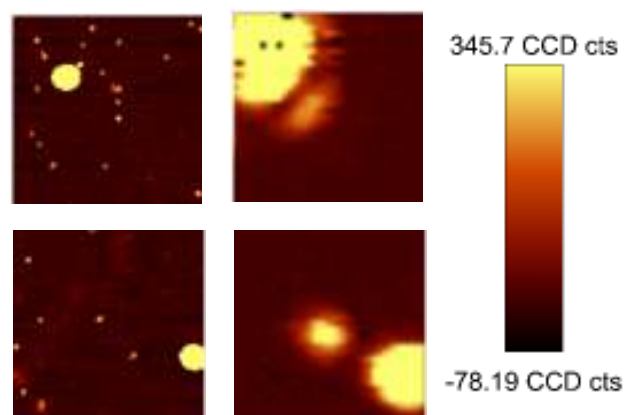


Figure 2.7: AFM (left) and Confocal Raman (right) images of 50 nm colloid on 20 nm film with poly-4-vinylpyridine spacer

The regions of large signal seen in the top left and bottom right corners of the confocal Raman image correspond to the two nanoshells seen in the AFM image. The source of the secondary bright spot seen in both images is unclear, but it clearly does not correlate to any of the colloid visible in the AFM scans. The Raman image was generated by obtaining a complete spectrum at each pixel with an integration time of three seconds, and using the intensity of the 1077 peak, integrated from 1050 rel. 1/cm to 1100 rel. 1/cm., of para-mercaptoaniline to generate a Raman intensity at each pixel.

While the nanoshells show the enhancement expected from isolated nanoshells, none of the colloid that appear in the AFM image show any Raman signal at all, indicating no, or extremely weak, enhancement of the incident electric field. It should be noted that the nanoshells show good enhancement at the wavelength expected for isolated nanoshells because, even though the plasmon of the thin gold film and the plasmon of the nanoshell probably couple to some extent, this coupling does not cause the disappearance of the isolated nanoshell plasmon, but merely generates a hybrid peak at lower energies

[27]. The 50 nm colloid on the 20 nm film exhibits little to no enhancement of the Raman scattering of para-mercaptoaniline.

The picture changes drastically when 80 nm colloid is used instead of the 50 nm colloid. As is clear in Figure 2.8, a Raman signal is obtainable from each individual colloid. Although the signal is still perhaps too weak for widescale imaging in this sort of setup, there are various solutions which can be implemented, which will be discussed in a later section. The important observation is that a strong enhancement of the Raman signal of the para-mercaptoaniline is visible on a three second time scale when 80 nm colloid is deposited over a 20 nm thin gold film.

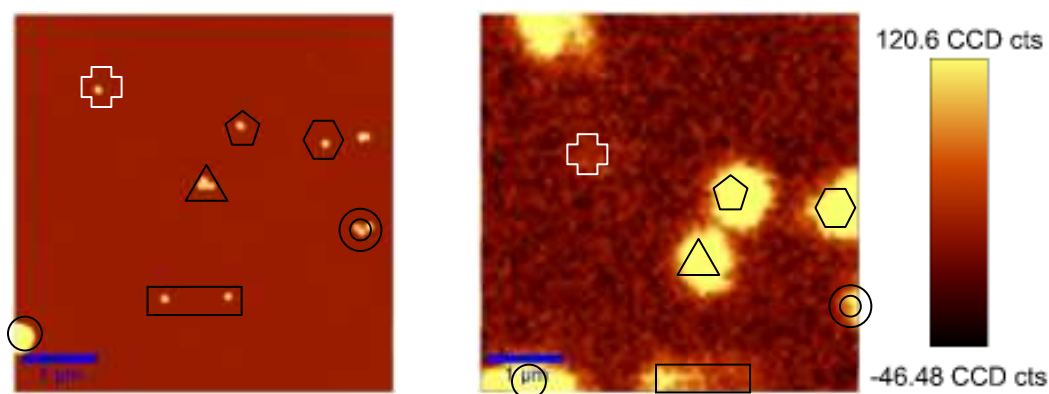


Figure 2.8: AFM (left) and Raman (right) images of 80 nm colloid over 20 nm film with poly-4-vinylpyridine spacer, shapes added to illustrate correlation.

The bright spot in the bottom left corner is clearly correlated with a nanoshell, and the lower of the two center bright spots is generated by a small aggregate of colloid, however, the rest of the signals seen in the Raman image all correlate to single, isolated, colloid. There is a small offset as the alignment procedure does suffer from some small inaccuracies, which explains why the bright area does not correlate to any single colloid in the AFM image in Figure 2.8, which is most likely another single gold colloid when

the Raman image is compared with the top AFM image of Figure 2.6, but the correlation between the AFM image and the confocal Raman image should be clear. The image was generated in the same manner as the Raman image for 50 nm colloid over 20 nm film, that is the full spectrum was collected, but only the 1077 peak was used in generating the image. The integration time and laser power were also the same. The integration time is set on the instrument while the laser power was adjusted by observing the strength of the Rayleigh, the elastic scattering, peak in the spectrometer because of the lack of a power meter for the laser. Because both samples have a background with the same reflectivity, the thin gold film, the strength of the Rayleigh peak should provide a good judge of relative laser strength, as Rayleigh scattering is directly proportional to the incident intensity. When the colloid used is changed from 50 nm to 80 nm, the Raman signal strength increases greatly and Raman imaging becomes a possibility.

2.7.2 PMA Spacer and Analyte

An interesting phenomenon that arises is the fact that some nanoparticles exhibit a clear Raman signal, for instance the pentagon and hexagon in Figure 2.8, while other nanoparticles are almost devoid of any signal, for example the cross in Figure 2.8. The most likely explanation of this is that the cross is not a gold nanoparticle, but an artifact of para-mercaptoaniline deposition, as shown in Figure 2.9.

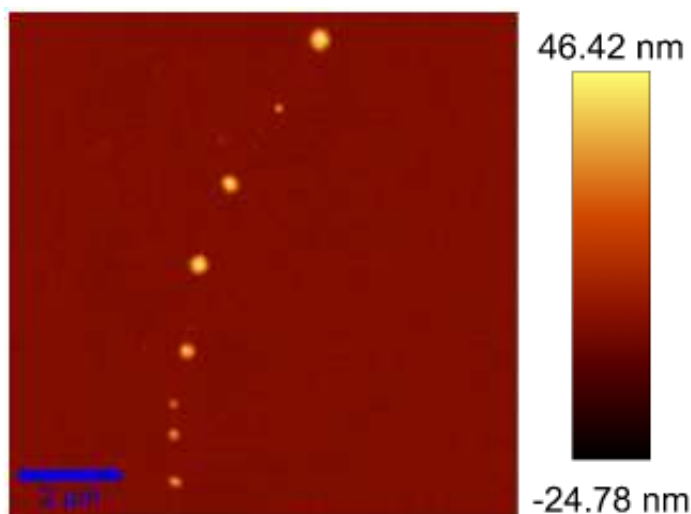


Figure 2.9: AFM image of para-mercaptoaniline on a 20 nm gold film

Because of the appearance of non-metallic artifacts, and to enhance signal strength from individual nanoparticles, the poly-4-vinylpyridine spacer layer was removed and para-mercaptoaniline was used as both the spacer layer and the analyte. To verify which particles are metallic and which are not, SEM was also performed on samples after AFM and Raman images were obtained. The 80 nm nanoparticles on a 20 nm film were favored for this experiment, since this combination displayed the greatest signal from the previous experiments.

As shown in Figure 2.10, any metallic particle-like features on the sample exhibit a pronounced Raman signal. The images were generated by integrating about the same wavenumbers as in the earlier figures. Because of the larger signal strength resulting from removing the poly-4-vinylpyridine spacer layer, the integration time used for these experiments was easily reduced to one second at the same laser power.

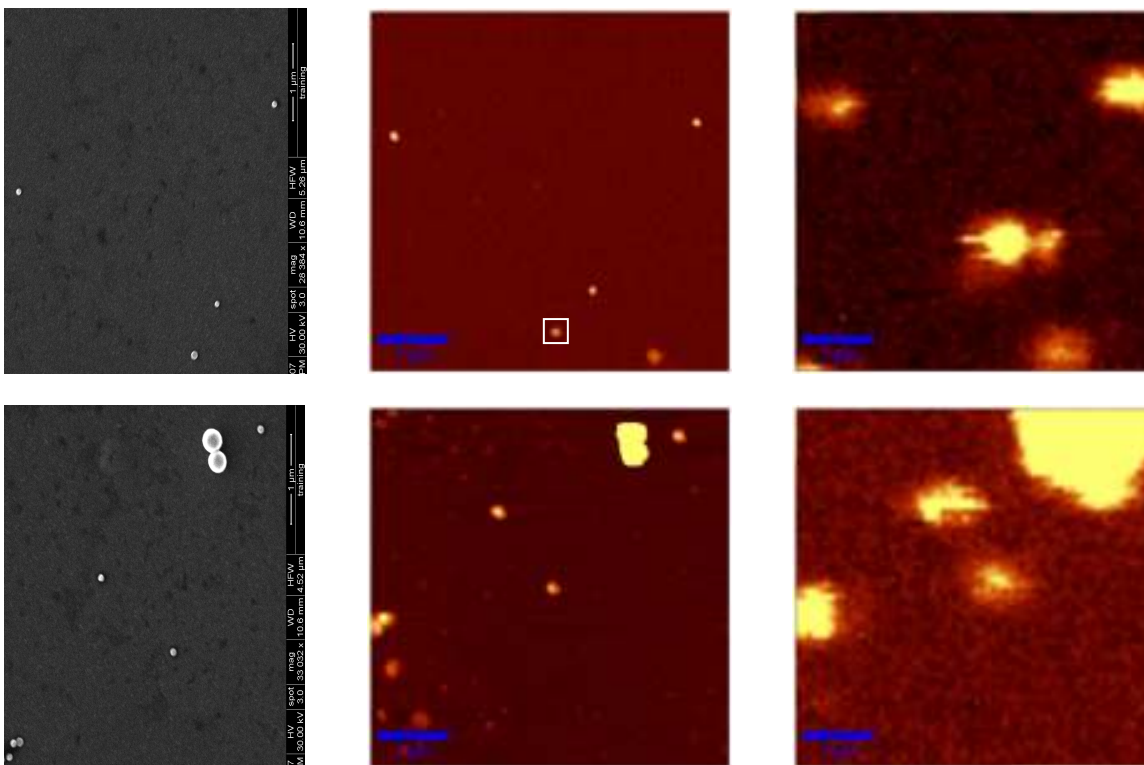


Figure 2.10: SEM (Top and Bottom Left), AFM (Top and Bottom Middle) and Raman (Top and Bottom Right), of 80 nm nanoparticles on 20 nm gold film with no poly-4-vinylpyridine spacer.

With a much larger and clearer Raman signal, it is more reasonable to compare intensities between different particles. In the top series of images in Figure 2.10, one feature of interest is that the bottom most nanoparticle, marked with a square, exhibits a lower maximum signal strength than the other nanoparticles in the image. Careful examination of the AFM and SEM images shows that this particle may be more disk-like in nature compared to the other nanoparticles, resulting in a lower enhancement in the junction. To confirm this hypothesis, Matlab was used to obtain a variety of cross-sections on this particle and another one in the image. These results are shown in Figure 2.11.

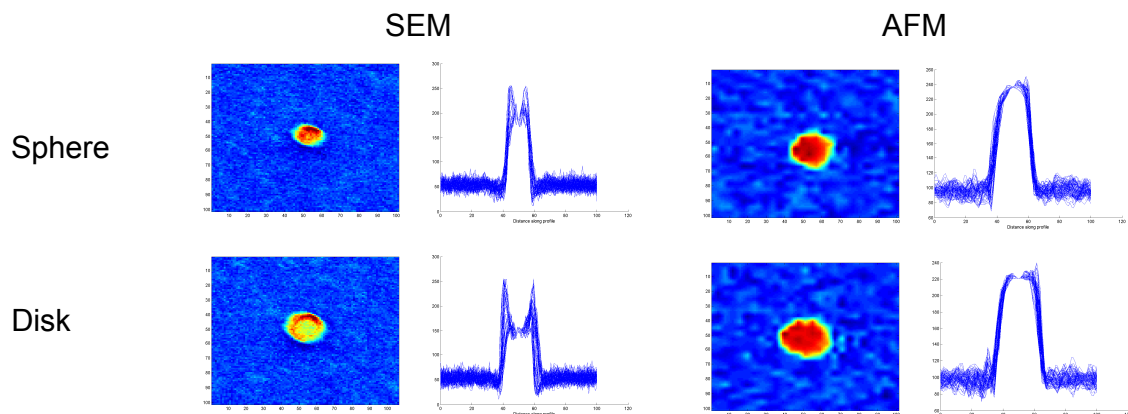


Figure 2.11: Matlab cross-sections of the sphere (top row), and disk (bottom row), performed on the SEM (left column) and AFM (right column) images.

As seen in Figure 2.11, the particle in question is definitely more of a disk than a sphere, which shows how critical the shape of the particle is to the amount of enhancement in the nanoparticle-thin film junction. While this has not been explored further, the tuning of nanoparticle shape provides for another level of control in the nanoparticle over thin metallic film geometry for surface enhanced Raman applications.

2.8 Discussion

Enhancement from a colloid on film system is clearly demonstrated above, however, some questions still remain. First of all, the enhancement is much weaker than expected, and is in fact nonexistent for 50 nm colloid on 20 nm film. While the location of the coupling peak depends on the size of the colloid as well as the thickness of the film, theoretical calculations and previous experiments [27] indicate that there should be some enhancement at an incident wavelength of 785 nm on a 50 nm colloid and 20 nm film sample. There are a variety of reasons why these limitations have appeared.

First of all, as noted earlier, perpendicular incidence of the laser is not the ideal way to excite a sample with this geometry. While there is a component of the incident electric field perpendicular to the sample surface generated by focusing the laser, ideally the majority, or all, of the power would be polarized in this direction. Therefore, changing the direction of incidence from perpendicular to the sample to a grazing incidence should increase the signal strength. This idea is supported by previous experiments [27] where the strength of the junction plasmon increases with a lower angle of incidence. There are improvements in other areas that may lead to the signal strength we would expect for a sample of this geometry.

Although the nonideal direction of laser has stood in the way of obtaining perfect results, these results are nonetheless still promising. Enhancement is clearly observed for 80 nm colloid over 20 nm film while it is completely absent for 50 nm colloid over 20 nm film. This dependence of enhancement on colloid size and shape allows for precise engineering of surface-probe geometries for use in improving current implementations of NSOM spectroscopy and making imaging a wide range of samples a distinct possibility.

Chapter 3

Work Function STM of palladium coated gold nanoparticles

3.1 Scanning Tunneling Microscopy

Before the development of the modern scanning tunneling microscope (STM), Young at what was then the National Bureau of Standards (now the National Institute of Standards and Technology, or NIST) invented what could be considered the direct precursor of the STM, the topografiner [33, 34]. Although its method of operation, namely raster scanning a sample in the x-y plane and recording information along the z-axis, is similar to how STMs operate nowadays, Young was unable to push the topografiner from the field emission regime into the tunneling regime [33]. In the field emission regime, a relatively high voltage, on the order of a few kV, is applied between the tip and the sample, which are separated about 1000 Ångstroms [33]. This voltage is high enough to cause the tip to emit electrons into the sample, which results in a current that can be used for imaging [33]. Although this represented a large leap forward at the time, Young's topografiner was limited to a resolution of about 30 Ångstroms perpendicular to the sample and about 4000 Ångstroms in the plane of the sample [34]. Young came close to developing a true STM, needing only to solve vibration issues that prevented positioning the tip within Ångstroms of the sample, but NIST cancelled his project and this opportunity was left for others to pursue [33, 34].

The STM was developed at IBM by Binnig and Rohrer in 1982 [33-34]. While the first modern STM experiments consisted of the generation of log I - s plots with a tungsten tip over platinum in 1981 [33], where I is the current and s is the tip-sample separation, STM's first major breakthrough was revealing the structure of Si(111) 7x7 in

the autumn of 1982, a long outstanding question in the world of surface science at the time [33-34]. Since then, the STM has found a great deal of utility in many different surface science applications. Binnig and Rohrer were awarded the Nobel Prize for this invention in 1986.

In the following sections, a basic introduction to the theory of STM will be presented. A more detailed explanation of the technique pertinent to this document, dI/dZ imaging, will also be expanded upon.

3.2 Basic STM Theory

A basic understanding of the operation of the STM can be garnered by reviewing the phenomenon of quantum mechanical tunneling through a square barrier. Classically, when a particle encounters a potential barrier, there is no possibility that this particle passes through the barrier resulting in 100% reflection. In quantum mechanics, however, the wave function of the particle is non-zero on the other side of potential barrier, and in the case of a thin barrier the particle has a significant chance of tunneling through and appearing on the other side. Because of the units associated with the exponential dependence of tunneling current on barrier width, the resolution of an STM can be on the order of picometers. Given the sensitivity of the measurement, equally precise positioning and signal acquisition must accompany the fundamental physics. However, it is important to remember that the STM generates an image that is a convolution of topographic and electronic states and that this convolution reflects and interplay of both the tip and sample density of states.

3.3 dI/dZ Spectroscopy

STM, in its most common configuration, provides extremely high resolution topographic and electronic information, but lacks a great deal of chemical specificity. Work function based spectroscopy and imaging can provide such information to some degree by allowing for the extraction of local barrier height energies from the surface of interest.

Bulk work function measurements have been investigated for over a century and have progressed further with the development of ultra-high vacuum techniques (UHV) [35]. Conventional methods of measuring work function, such as the Kelvin probe method, provide work function information on a macroscopic scale. More recent techniques have improved the resolution of work function data collection. Focused local electron probes and photoemission electron microscopy [35] both push resolution into the micron range, and Kelvin probe force microscopy (which uses an atomic force microscope and the Kelvin probe method) improves resolution further into the submicron regime [35].

The local barrier height is of great interest because of the degree to which surface properties affect the work function. For instance, the bulk work function depends on which surface of a metal is exposed. In the case of copper, the (111) surface of copper shows a different bulk work function than the (110) surface because of the arrangement of surface atoms [35]. Other local features, such as adsorbed atoms or steps on the surface, can also change the observed bulk work function [35].

To understand how to extract such information, one must start from the expression for tunneling current in the case of the 1-D square barrier, where [33, 35, 36]:

$$I \propto e^{-2z\sqrt{2m\phi}/\hbar} \quad (4.1)$$

and rearranging the terms into the form, where the constant has units of Ångstroms*eV:

$$\Phi = 0.95\left(\frac{1}{I} \frac{dI}{dz}\right)^2 \quad (4.2)$$

the extraction of the work function value from an STM measurement becomes mathematically straightforward.

One must now apply this mathematical expression to experimentally measured properties. A basic diagram of the setup is shown in Figure 3.1. A lock-in amplifier provides a small voltage modulation at a known frequency on the z-piezo of the STM. The magnitude of this modulation is directly convertible into the dZ term. The lock-in amplifier processes the resulting current signal and outputs the magnitude of the current at the reference frequency. This value is proportional to the dI term. The current term, I , is set by the user during imaging. These values fit directly into the equations above to give us the value of the work function at each point on the surface of interest.

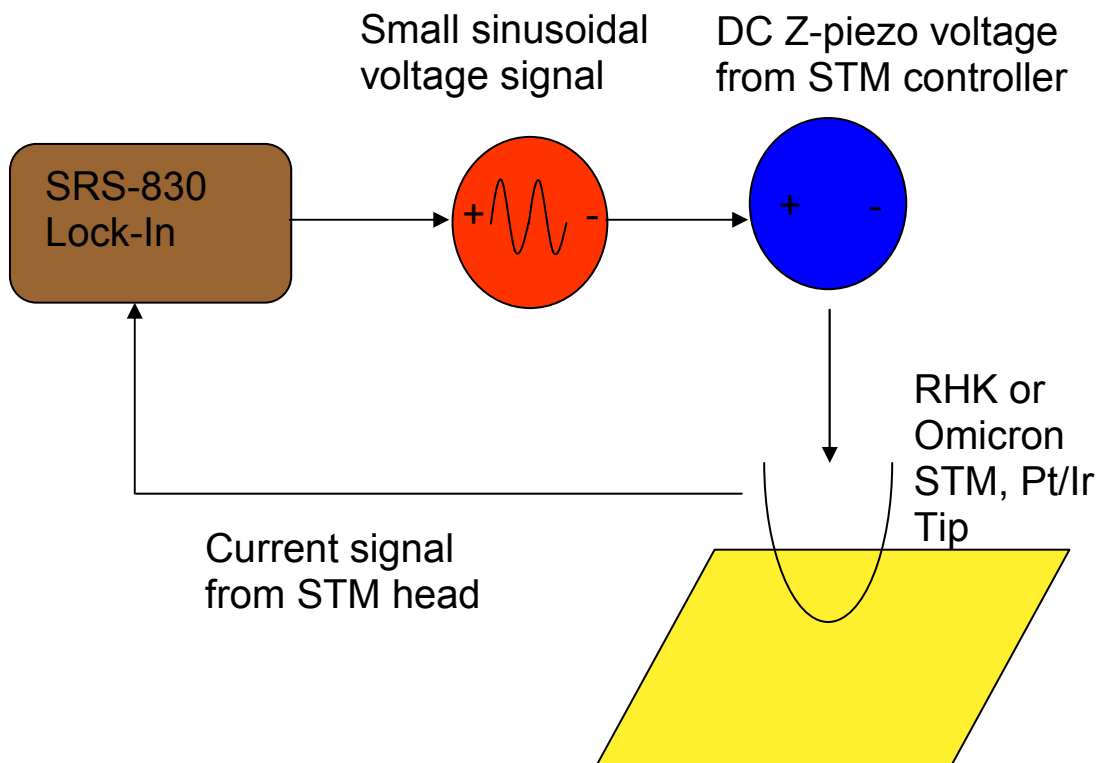


Figure 3.1: Basic dI/dZ STM setup

dI/dZ spectroscopy has been used to study a wide variety of substrates, and will be shown to be a very powerful technique for the analysis of the surface of nanoparticles.

3.4 Self-Assembled Monolayers

A self-assembled monolayer is a thin film of a molecule on a surface that spontaneously constructs itself through surface-molecule interactions and terminates predictably, typically at one layer of the molecule. Because of the predictable and well defined ordering of SAMs, their utility has been quite pronounced in research. While a large database [37] of metal-functional group pairs exists for determining what will result

in a SAM, for the purposes of this chapter we are most interested in alkanethiol SAMs on gold and palladium.

Alkanethiol SAMs on gold have been well studied. The sulfur in the thiol group forms a bond (~ 44 kcal/mol [37]) with the gold surface, and the nonreactive methyl group at the other end of the alkane chain prevents any further reactions. These SAMs have a few different phases, many of which involve alkane chains that are “laying down” on the surface [38]. The exact geometry of these “laying down” phases is determined by the alkanethiol surface coverage. At a certain concentration of molecules on the surface, the alkane chains of the molecules rise from the surface and form a close packed, hexagonally arranged, array of alkane chains that stand up from the surface, to which they are bound with the sulfur atom, at a 30° angle. The molecules are positioned such that they form a $(\sqrt{3} \times \sqrt{3})R30^\circ$ overlayer structure on the gold, as seen in the schematic in Figure 3.2. [37]. Figure 3.3 shows a variety of STM images of alkanethiol SAMs on gold. From these images, the formation of well ordered domains and the appearance of SAMs at surface coverages insufficient to cause the formation of a traditional SAM should be clear.

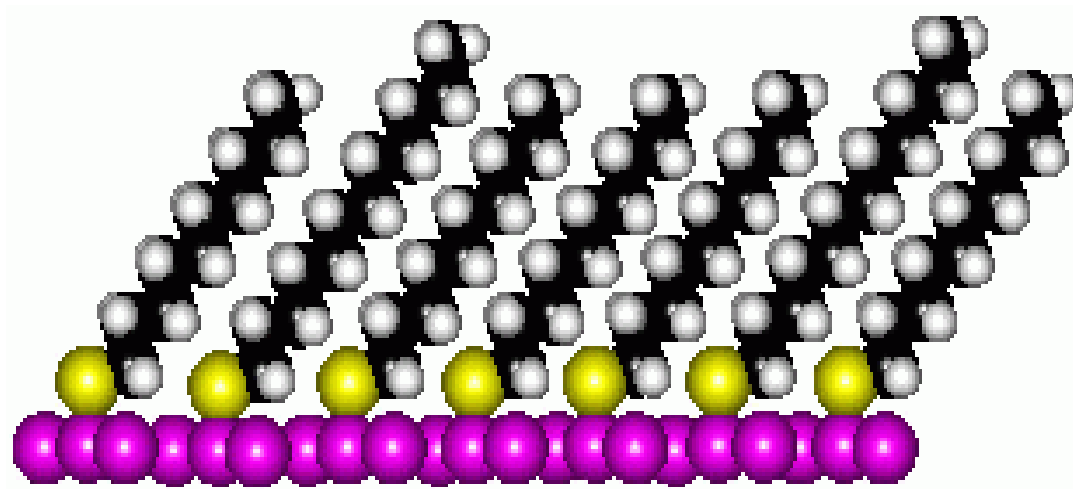


Figure 3.2: Side-view schematic of an alkanethiolate SAM on Au. Purple represents gold, yellow sulfur, black the carbon backbone of the alkanethiol, and white hydrogen.

A variety of potential defects in alkanethiolate SAMs on gold exist. SAMs on gold typically form in macroscopic domains, where all of the alkane chains are tiled in a particular direction. These domains are easily visible in Figure 3.3. One common defect is the boundary between domains, where the ordering is not as tight packed as it would be within a domain. Another common defect is a vacancy within the SAM lattice. While the term defect connotes an undesirable effect, defects in SAMs can be exploited for novel methods of study.

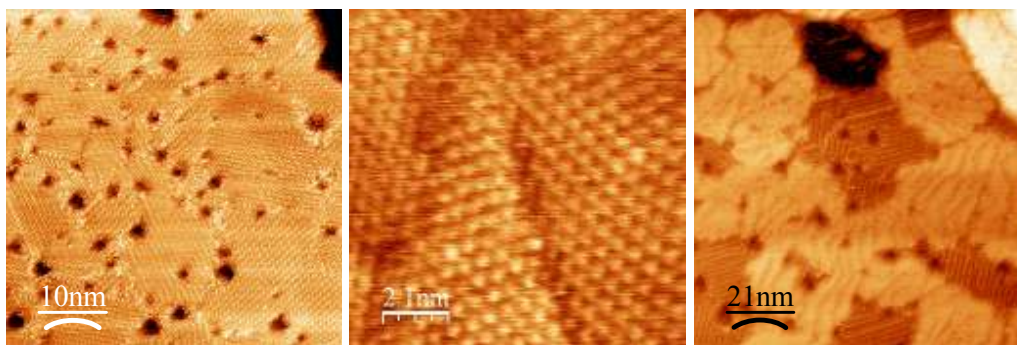


Figure 3.3: Left: STM of hexanethiolate SAM on gold, center: STM of decanethiolate SAM on gold, right: STM of decanethiolate SAM on gold showing lower concentration domains

SAMs have seen a large variety of uses in experimental research. The patterning of SAMs allows for a number of potential mask applications [37]. Molecules of interest have been inserted into defects in a SAM, allowing for the isolated study of a single molecule [39-41]. Stacked SAM layers, utilizing end group chemistry to allow for the stacking of layers, have allowed for the fabrication of gaps in structures that are smaller, faster, and simpler to fabricate than with other existing methods [42-44]. For the purposes of this document, the use of entangled alkane chains for the immobilization of nanoparticles, a process similar to the insertion of molecules in SAM vacancies, is of immediate interest.

3.5 Motivation

Palladium has always been a metal of interest, especially for catalytic purposes. One specific application, the hydrodechlorination (HDC) of tetrachloroethene (TCE), is of great interest in controlling water pollution and removing this toxin from the environment [45-48]. Recent developments in the synthesis of palladium coated nanoparticles have expanded the possibilities for palladium's catalytic activity. While the

catalytic role of palladium in HDC reactions has been studied in many forms, the development of gold core-palladium shell (Au/Pd) nanoparticles represents a potential breakthrough in catalytic efficiency. Compared with Pd on Al_2O_3 and pure Pd nanoparticles, the gold/palladium nanoparticles show a great increase in catalytic activity [45-48]. Au/Pd nanoparticles also exhibit resistance to common species known to deactivate other Pd catalyst geometries [45]. Maximum catalytic activity also appears to occur at sub-monolayer coverage of the gold shell, which makes understanding the surface structure critical to the widespread application of Au/Pd nanoparticles [46]. While the structure of these particles has been studied through transmission electron microscopy and x-ray absorption spectroscopy [47], a better understanding of the exact structure, especially the surface of these nanoparticles would be helpful. Toward this end, a powerful method for obtaining this information is dI/dZ imaging through STM.

STM, when imaging dI/dZ signal, has been used in the past to determine the work function of various areas of a sample. As described above in section 4.1, when a small voltage modulation is applied to the Z-piezo of the scan head, and the resulting current modulation is read through a lock-in amplifier, the dI/dZ signal is obtained. This dI/dZ signal is directly related to the work function through the relation detailed in Chapter 3. Through this relation, we can directly probe the surface of the nanoparticles to differentiate between gold, palladium, some alloy, or potentially some surface coverage percentage.

This chapter will demonstrate this STM technique and better reveal the surface structure of these palladium coated nanoparticles.

3.6 Experimental Setup

As shown in Figure 3.1, a small AC voltage signal is applied from a lock-in amplifier to the STM head. The resulting current signal is then processed by the lock-in amplifier, which generates the amplitude of the dI/dZ signal. This process is performed at every pixel of the STM image, which results in a dI/dZ image. This series of experiments was performed in a commercial RHK UHV STM or commercial Omicron UHV STM system with a lock-in amplifier from Stanford Instruments. Pt/Ir tips were mechanically sharpened before use.

Palladium and gold-coated palladium particles, generally a few nanometers in diameter, were obtained from the Wong group at Rice University. 15 nm gold nanoparticles were purchased from Ted Pella. Because nanoparticles of these sizes are rather prone to moving around on a surface during STM measurements, the particles were functionalized with an alkanethiol (decanethiol) self-assembled monolayer. A SAM was also created on the gold substrate that these particles were drop cast onto, which results in an entanglement effect. This entanglement of alkane chains, which is diagramed in Figure 3.4, helps to immobilize the nanoparticles enough to obtain some measurements from these samples.

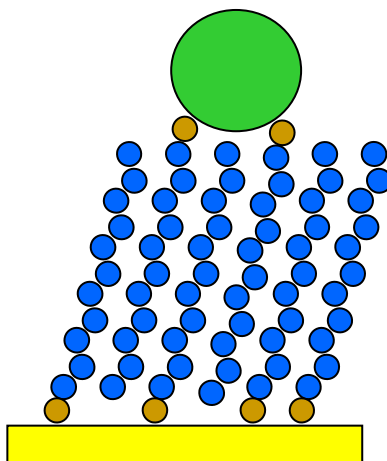


Figure 3.4: Schematic of the entanglement process between a nanoparticle and a SAM

Although individual spectrum from targeted nanoparticles would be ideal, as will become apparent later in the chapter, even with entangled alkane chains, the particles still move around significantly during an STM scan and specific targeting becomes near impossible. Because of this particle movement, the best way to extract work function information is to obtain a full dI/dZ image, locate the particles in the image, and extract the appropriate values required to calculate the work function of the particles of interest. For this purpose, MATLAB was used to find an average of the dI/dZ value in the neighborhood of the center of the nanoparticles found, and this value was used to calculate the work function.

3.7 Experimental Results

Early experiments were aimed at obtaining single I/Z spectra from individual particles, then extracting dI/dZ from this line and calculating a work function from this value. Unfortunately, in practice, nanoparticles of this nature are still somewhat mobile even with SAM entanglement (see Figures 3.5-3.7) and obtaining a spectrum from the

nanoparticle of choice becomes extremely difficult. For this reason, the change to dI/dZ imaging was made, where the dI/dZ value is directly obtained from the image.

Shown in Figure 3.5 is a fairly representative image of what is observed when scanning 15 nm Au nanoparticles on a decanethiolate SAM. Although there are some large clumps of nanoparticles evident on the surface, there are enough isolated nanoparticles to extract reasonable dI/dZ values from. Qualitatively, the value of the work function on these nanoparticles is higher than the value over the background SAM.

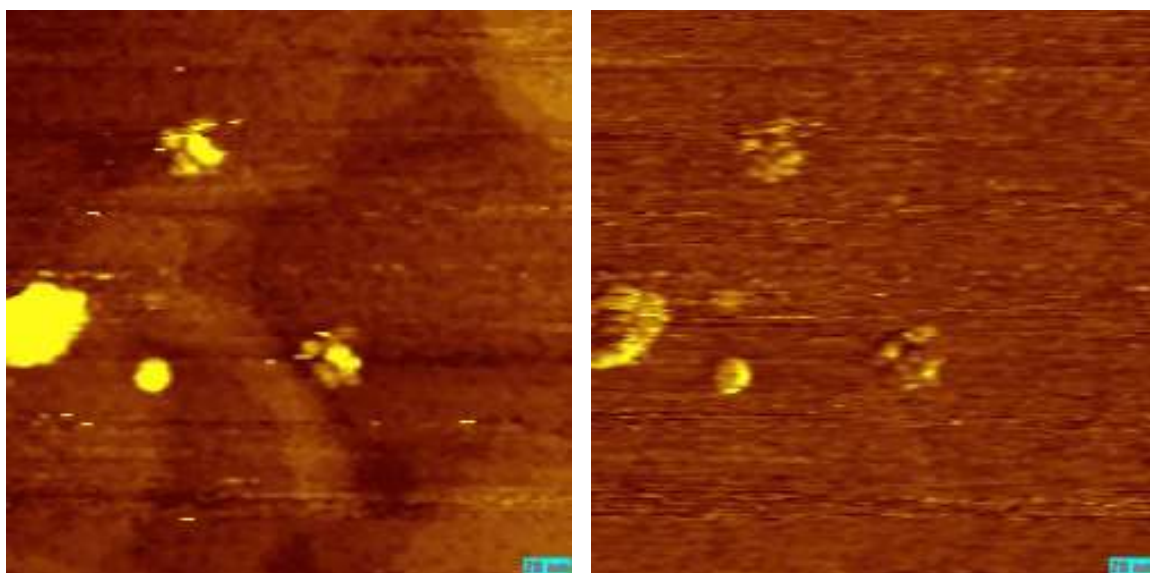


Figure 3.5: Topography (left) and work function (right) images of Au nanoparticles entangled onto a decanethiolate SAM.

Figure 3.6 displays what is commonly observed for Pd nanoparticles. This image shows the mobility of these nanoparticles more clearly and illustrates the necessity of dI/dZ imaging over attempting to obtain single spectra over targeted nanoparticles. The work function on the Pd nanoparticles appears to be slightly lower than that of the background SAM. Although the work function of bare Pd is slightly higher than that of

bare Au, the presence of the SAM is expected to alter the measured work function value in a dI/dZ image, so this result is not surprising.

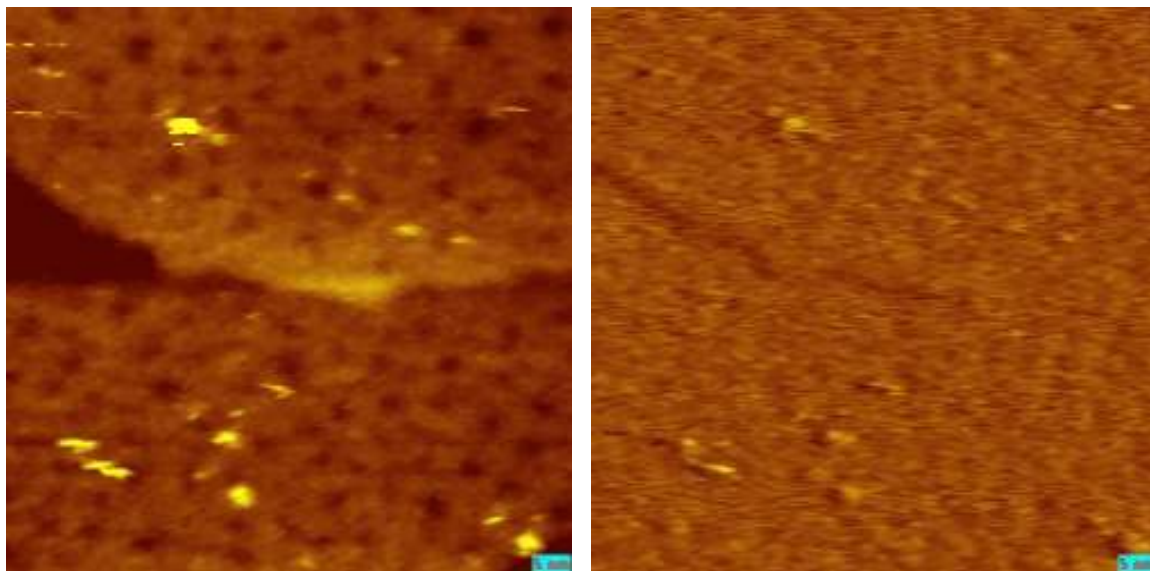


Figure 3.6: Topography (left) and work function (right) images of Pd nanoparticles entangled onto a decanethiolate SAM

For the nanoparticles of interest, the AuPd nanoparticles, the topography and dI/dZ images are shown in Figure 3.7. Upon inspection, the work function images of these nanoparticles more closely resembles those of the Pd nanoparticles in that the particles show up as lower in dI/dZ value than the underlying decanethiolate SAM. Without any sort of quantitative calculations, the Pd nature of these particles is clear.

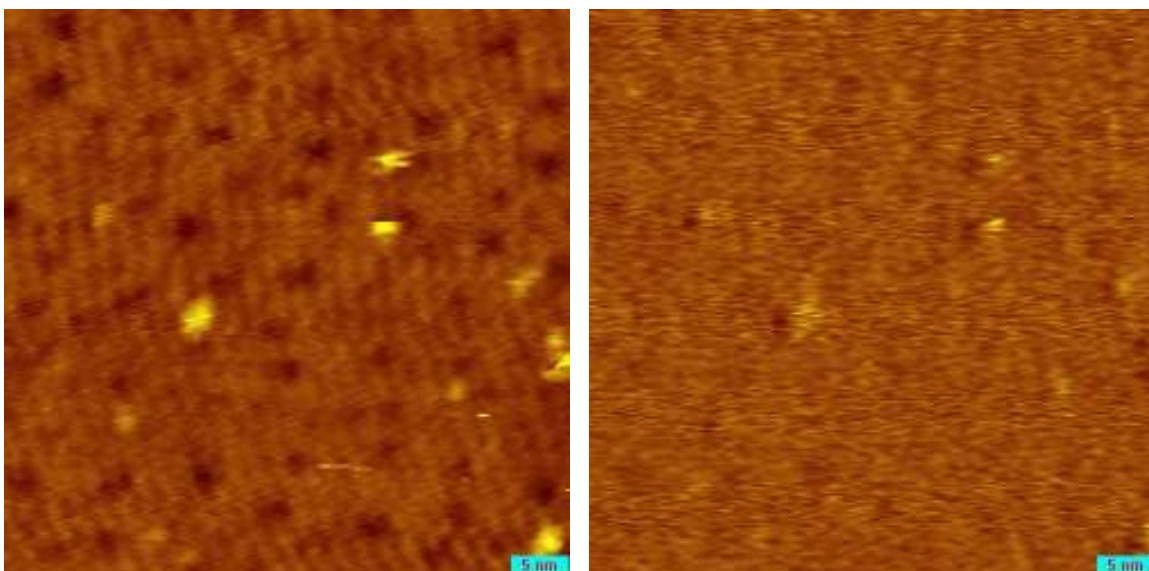


Figure 3.7: Topography (left) and work function (right) images of AuPd nanoparticles entangled onto a decanethiolate SAM.

The amount of information gathered without performing any calculations is extraordinarily limited, as shown above. For this reason, a MATLAB program was written that averages the values of a 3 pixel x 3 pixel area selected by the user. This program was used to obtain the values used in a more quantitative comparison. Particle work function is normalized by the SAM work function obtained in the local area in order to remove any instrument specific parameters.

Table 4.1 shows the values extracted from various Au, Pd, and AuPd nanoparticles. These values have been normalized to the work function extracted from the local SAM to remove any tip effects that may have appeared during measurements. Not surprisingly, based on the qualitative examination of the images above, the work function value for the Au nanoparticles comes out to be slightly higher than the background SAM. The values from Pd nanoparticles, in accordance with the qualitative examination of the images in Figure 3.7, show that the work function of the Pd

nanoparticles is slightly lower than the work function of the local decanethiolate SAM. Again in a qualitative match, the values for these nanoparticles is slightly below the background decanethiolate SAM, however, the values are consistently slightly higher than those of the Pd nanoparticles.

Au	Mean (particle Φ /substrate Φ) 1.27 Std. Dev. 0.37	32 particles
Pd	Mean (particle Φ /substrate Φ) 0.90 Std Dev. 0.08	24 particles
AuPd	Mean (particle Φ /substrate Φ) 0.96 Std. Dev. 0.02	47 particles

Table 3.1: Mean and standard deviation of the work function ratio (over particle/over substrate) for the various nanoparticles studied.

The values from the table above seems to indicate that while the AuPd nanoparticles are more Pd like on the surface than Au like, some of the core Au nature of these nanoparticles appears to be showing through. The most likely explanation is that the Pd coating is not completely covering the underlying Au core, which would cause the average reading for the particle to jump up a very small amount relative to a straight Pd nanoparticle.

3.8 Discussion and Conclusions

From the dI/dZ images obtained, the work function of Au nanoparticles is expected to be slightly higher, and the work functions of Pd and AuPd nanoparticles is expected to be slightly lower than the underlying decanethiolate SAM. The extracted numbers further support this conclusion while adding in a small increase in the work function in the AuPd nanoparticles when compared to Pd nanoparticles.

Some confusion may arise because the work functions of Au(111) and Pd are quite close together, 5.31 eV and 5.12 eV respectively [49]. The divergence of the values from the expected bare nanoparticles values can be explained by noticing that the work function being measured is not that of the bare metal, but of a metal functionalized with a SAM. Alkanethiolate SAMs on Au have been shown to reduce the observed work function by about 1 eV, with slightly larger reductions for longer chain alkanethiols [50-51]. This work function reduction has been shown to be dependent on the choice of metal as well, as the observed work function reduction is smaller for an alkanethiolate SAM on Ag [51]. Therefore, the differences that arise in the relative work function values between the SAM on gold and the SAM on palladium is most likely due to the differing interaction strength between the decanethiol molecule with gold and the decanethiol molecule with palladium.

The difference between the values on the gold nanoparticles and the gold substrate could be explained by a difference in interaction strength between decanethiol and amorphous gold and decanethiol with Au(111). Surface morphologies could also explain this difference, for instance, the local work function of a surface is slightly lower at a step edge because of the Smoluchowski effect [35]. Because the local shape of the

surface influences the observed work function, the size and shape of the nanoparticles could play a factor in changing interaction strength when compared to a flat plane of gold.

The small increase between AuPd from Pd values is most likely due to a slightly incomplete Pd coverage of the underlying gold particle. Since the MATLAB algorithm averages 9 pixels along the particle in order to obtain a more stable reading, small irregularities in the surface would be expected to arise in this manner. Regardless of this fact, however, the surface appears to be much closer to what is expected for palladium, and is more than likely nearly completely covered by palladium.

While work function imaging in STM has been demonstrated to be able to differentiate between Au, Pd, and AuPd nanoparticles, some measures exist to further reinforce the results of this experiment. In the near term, taking measures to ensure a cleaner tip would help to obtain more decisive results, especially for the images since the contrast is less clear than ideal. A different immobilization strategy would help as well, since covering the entire particle and probing the SAM that exists on the particle is not the best scenario. These options are explored in more detail in Chapter 6.

Chapter 4

Raman Imaging of Nitrogen Doped Graphene

4.1 Graphene

Over recent years, sp^2 bonded carbon has generated a lot of interest because of its unique properties which vary greatly on geometry. The basic form of sp^2 bonded carbon is graphene, which is essentially a single layer of sp^2 bonded carbon atoms. From this basic structure many different geometries arise, including but not limited to carbon nanotubes (rolled up graphene sheets), nanoribbons (thin strips of graphene), multilayer graphene, and the old standby, graphite (many layers of graphene stacked on top of each other) [52, 53]. Because the properties of sp^2 bonded carbon vary with geometry, all of these, and more, different structures have gathered a great deal of interest.

Graphene in and of itself is of particular interest because of the properties that arise from a single layer of sp^2 bonded carbon. The various structures allow access to studying physics in a controlled, well defined, $1D$ (nanotubes and nanoribbons), $2D$ (graphene sheets), and $0D$ (nanographite particles) setting [52]. Because graphene exhibits ballistic transport at room temperature, and because graphene exhibits a great deal of stability, future applications in electronics seem promising [53]. Studying graphene can also provide much information into other sp^2 bonded carbon structures, since these structures can be seen as derivatives of graphene [53].

Because graphene can be seen as the core unit behind all of these, and more, structures, the discovery of a method to isolate single layers of graphene via micromechanical cleavage [53] represented a promising avenue of research. Although determining the exact number of layers present can be experimentally tricky, some

success in this area has been seen with using optical examination on well calibrated SiO₂ substrates and by using atomic force microscopy (AFM) [53]. Because of Raman's historical success in analyzing sp^2 bonded carbon structures, and because of the details of graphene's Raman signature, Raman spectroscopy is an ideal candidate for more exhaustive optical analysis [52-53].

Raman spectroscopy has been used to analyze a large variety of sp^2 bonded carbon structures, including but not limited to graphite, fullerenes, and nanotubes [52]. Carbon compounds of this nature exhibit very specific characteristic Raman peaks, and graphene is no exception [52-53]. For this reason, further investigation into the use of Raman spectroscopy for the analysis of various graphene structures is of great interest.

4.2 Graphene Basics

As mentioned earlier, graphene is chemically a single layer of graphite. Graphene is composed solely of carbon atoms in a hexagonal pattern with all of the carbons sp^2 bonded to each other. Figure 4.1 displays this description graphically.

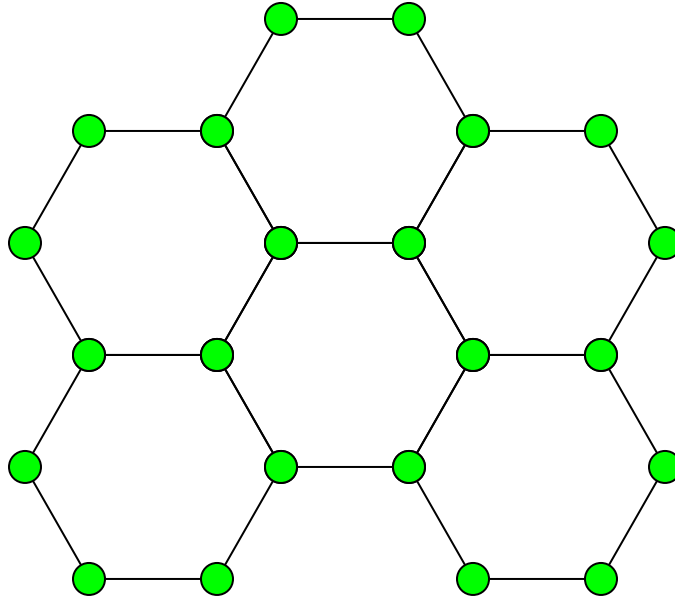


Figure 4.1: Pattern of carbon atoms in graphene

Because graphene is an extended system of π -bonds, it is expected to, and does exhibit remarkable unique electrical conductance compared to other forms of carbon. This structure also leads to a distinct Raman signature, as detailed in the next section, which is critical in producing and modifying graphene.

4.3 Graphene Raman

Ideal graphene has three distinct peaks, the strongest of which should occur at around 2400 rel. 1/cm. (G' or $2D$ peak). Graphene can also show a peak at around 1300 rel. 1/cm. (D peak) and another peak very close to 1600 (G peak), but for a single layer these two peaks should be as weak as possible.

The G' (also known as the $2D$) peak arises from a second-order two-phonon process, involving a phonon near the K point of graphene [52]. The incoming laser first generates an electron-hole pair. An electron-phonon scattering process occurs with an

exchanged momentum close to K . Another electron-phonon scattering process occurs with an exchanged momentum of the same magnitude, but opposite sign. At this point, electron-hole recombination occurs and a photon that has lost energy relative to the incoming laser is emitted [53]. As a result, the change in energy is equivalent to twice the energy of the scattering phonon. Figure 4.2 displays this process graphically, the energy level of the electron is neglected to simplify the diagram. This $2D$ peak is extremely sensitive to perturbations in the electronic or phonon structure of graphene and, unlike most Raman peaks, shows a dependence on incident laser wavelength [52]. Of particular interest is that this peak is extremely sensitive to the number of graphene layers present.

Because the $2D$ peak involved a true electronic excitation and resonant phonon decay processes, its shape and intensity are strongly dependent on the number of graphene layers present [53]. As more layers are added, the shape of the $2D$ peak evolves in a fashion that represents the addition of more resonant phonon channels [53]. The weakening of the $2D$ peak as more layers are added is most likely caused by the addition of non-resonant phonon decay channels. Because these channels would compete directly with the resonant, Raman active, phonons, the intensity of the $2D$ peak should decrease as more layers are added. Experimentally, this decrease is observed and at five graphene layers the spectrum is indistinguishable from graphite [53].

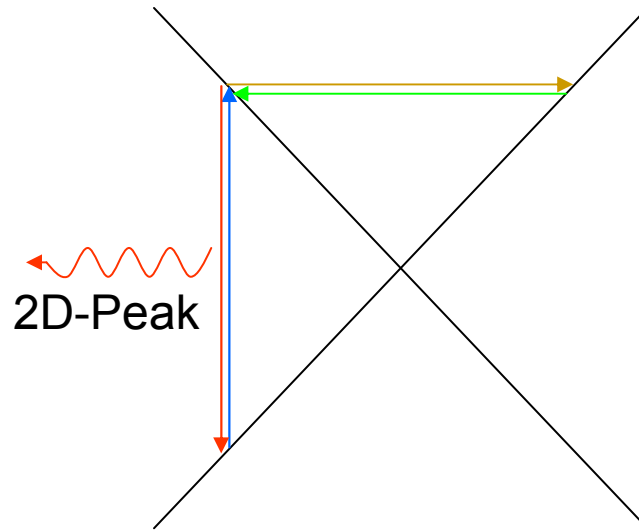


Figure 4.2: Energy level diagram of the origin of the $2D$ peak. The incoming laser excites an electron hole pair (blue). The first electron-phonon scattering event occurs (brown). The electron is scattered back by the same phonon (green). The electron relaxes back to the ground state, emitting the $2D$ peak photon (red).

The G peak is a characteristic peak of sp^2 bonded carbon compounds. This peak arises from C-C bond stretching, so all carbon compounds with extended sp^2 bonding, such as graphite and carbon nanotubes, exhibit a peak in this range [52]. Because of the nature of the origin of this peak, its exact properties are extremely sensitive to strain on the lattice, which, among other things, makes close examination of the G peak interesting for determining certain types of substrate interactions.

The D peak arises from a mechanism similar to the $2D$ peak. While the phonon that gives rise to this peak does not satisfy Raman selection rules in pristine sp^2 carbon samples, the presence of defects allows for this phonon to generate a Raman signal [53]. In the case of the D peak, however, the second scattering process is interrupted by a defect and the photon is released after only the first scattering process. For this reason, the shift of the D peak is roughly half of the shift observed for the $2D$ peak. See Figure 4.3 for a schematic illustration of the origin of the D .

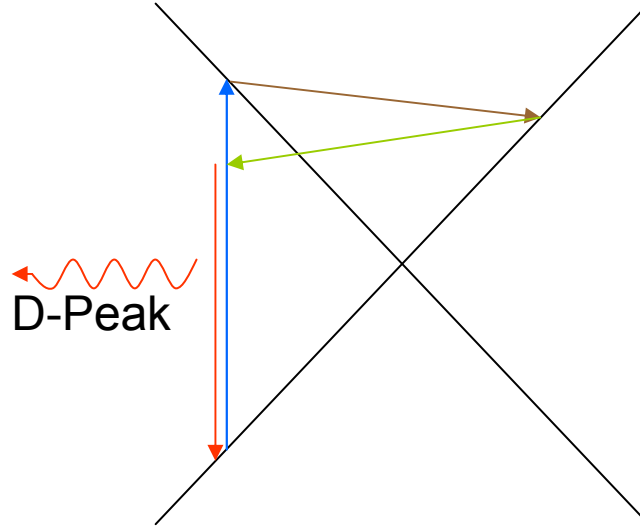


Figure 4.3: Energy level diagram of the origin of the *D* peak. The incoming laser excites an electron hole pair (blue). The first electron-phonon scattering event occurs (brown). The electron is scattered by a defect (green). The electron relaxes back to the ground state, emitting the *D* peak photon (red).

4.4 Doped Graphene

Doping refers to a process where some of the atoms in a bulk lattice are substituted by atoms other than carbon while preserving the sp^2 lattice structure. This procedure is well rooted in the modern semiconductor industry, because the doping of silicon allows for finer control and adjustment of properties, opening up a wider range of applications. Doped graphene is a critical field of research because of the promising properties of graphene.

Currently, commonly used dopants for graphene mainly consist of nitrogen (if introducing more electrons) or boron (if introducing more holes.) These elements were chosen because their nuclei are close in size to the carbon nucleus, which is important for

minimizing disruptions to the lattice. Disruptions that are too large would cause undesirable changes in graphene's properties.

Through doping graphene's chemical properties are changed. Electrical properties are changed, but more relevant to this document are the changes resulting in the Raman spectrum because of doping. Generally, the *D* peak will increase in intensity because these dopants act as intentionally added defects [54-55]. The *2D* peak will decrease in intensity for the same reason. The shape and location of the *G* peak change as well, for instance, in the case of nitrogen, the *G* peak splits into two distinct peaks with a small shift in the location depending on the amount of nitrogen added [54-55]. This document will explore these changes further in a later chapter.

4.5 Motivation

While undoped graphene already shows great promise in a variety of applications because of its high surface area, conductivity, and mechanical strength [56], recent advances in the ability to produce large samples of doped graphene has opened many opportunities in expanding graphene's potential usage and applications, for instance, semiconductor tuning [56] and Li battery electrodes [57]. To fully utilize doped graphene in practical applications, however, a method to determine the extent, homogeneity, and quality of doping must be developed.

Raman spectroscopy has historically proven to be a very powerful tool in the study of graphitic and graphene samples [52, 58-59] because of the sensitivity toward nanotube type (*G* peak), concentration of defects (*D* peak), and number of layers (*2D* peak). Because the Raman spectrum of graphene also changes with dopant type and

concentration, Raman spectroscopy shows a great deal of promise in analyzing these sorts of samples as well. Combined with two-dimensional imaging, which has been used in the past to analyze the quality and uniformity of graphene films, Raman imaging should prove to be a useful technique in the analysis of doped graphene films.

Earlier experiments on the Raman spectroscopy of N-doped graphene have focused on series of single spectra from bulk samples [54-56]. While correlation with different growth parameters allows for rough correlation between spectral features and Raman spectrum, inhomogeneous local doping can cause difficulty in attempting to qualitatively assign the strengths of different features of the Raman spectrum to dopant concentration. Raman imaging should provide a way to exactly determine how the Raman spectrum evolves with increased dopant concentration.

Toward this end, the Raman imaging of undoped and doped graphene is demonstrated and this data is analyzed in this chapter. Undoped graphene is scanned to determine a baseline of performance and establish reasonable expectations of results from the instrument, and doped graphene, specifically nitrogen-doped graphene, is the sample of actual interest. The differences in Raman characteristics between these samples will be demonstrated and the potential use of these differences in determining dopant homogeneity and concentration will be addressed.

4.6 Experimental Setup

The same WiTec instrument used for the experiments in Chapter 3 was also used, in the same configuration, for the Raman imaging of graphene. The same laser (785 nm) and objective (100x 0.9 NA Nikon) were also used. An area that looks visually suitable

in the standard optical microscope is targeted for AFM and Raman imaging, where a full Raman spectrum is obtained at every pixel of the image. The area is then raster scanned by AFM or Raman imaging. The spectral signal is passed through an Acton spectrometer and detected using an Andor CCD array.

One minor issue that arises is the fact that, because the detector is a silicon CCD array, the $2D$ peak is somewhat more suppressed because the magnitude of the shift from 785 nm places the $2D$ peak in a lower sensitivity region for silicon. Because comparing the strength of the $2D$ peak with the G peak is critical for determining the number of graphene layers, this issue does pose a small barrier. While this issue prohibits exact quantitative analysis of some of the features of interest, the capabilities and usefulness of Raman imaging for graphene applications should still be clear.

The graphene was prepared by the Ajayan group at Rice University. The graphene was initially grown on a copper substrate, and then transferred to indium-tin-oxide, which was purchased from SPI. Indium-tin-oxide was chosen because it is a clear and conductive substrate, which allows for future transmission and STM experiments. Although indium-tin-oxide exhibits a small fluorescence when excited with the 785 nm laser, this fluorescent background is small enough that the Raman signal from the graphene samples comes through clearly.

4.7 Experimental Results

As a test of the system's capabilities, Raman images of undoped graphene on ITO were obtained. The results of some of these scans are shown in Figure 4.4 below.

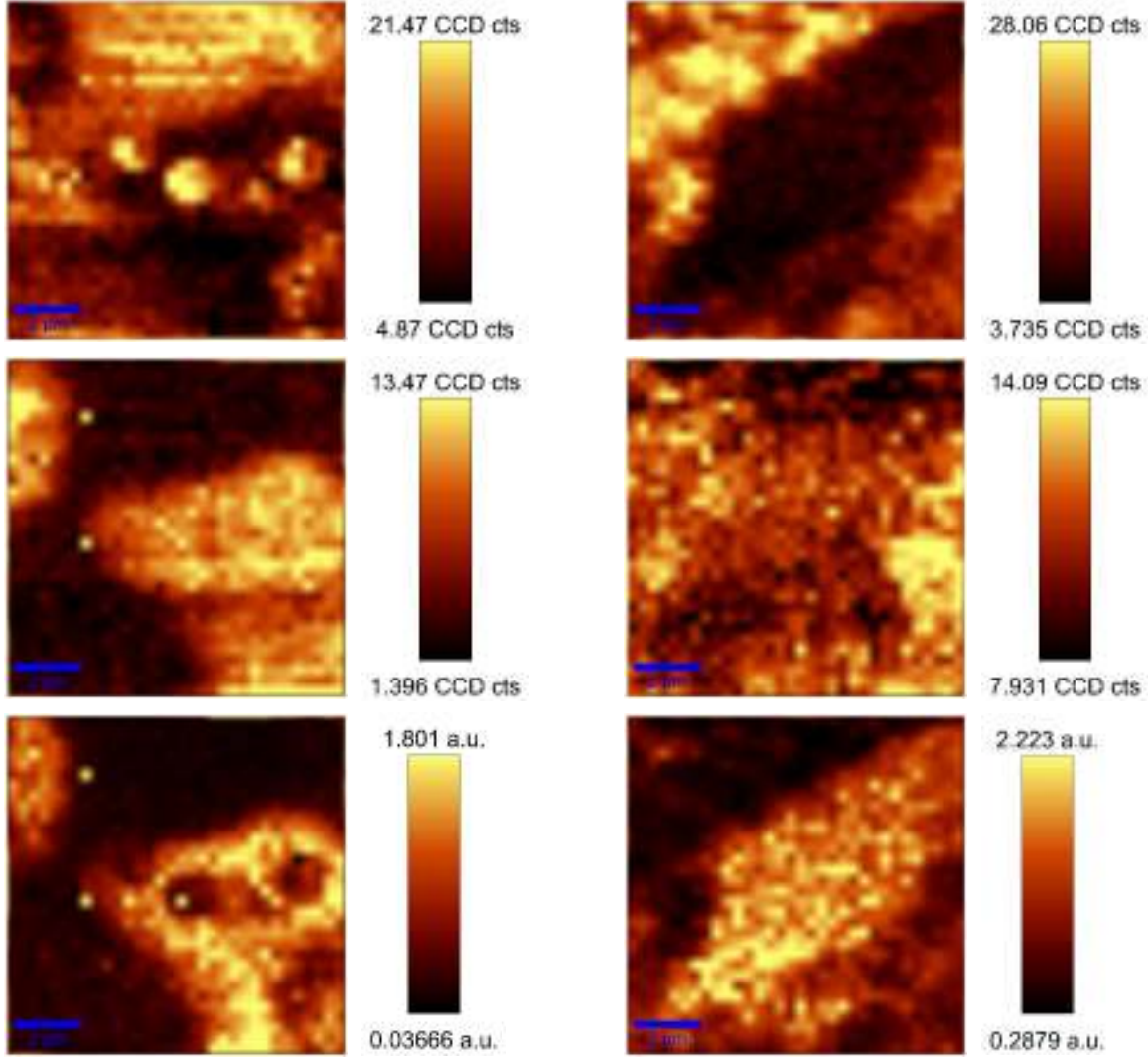


Figure 4.4: G peak (top), $2D$ peak (middle) and $2D/G$ ratio (bottom) for undoped graphene on ITO

In the left column of images, the intensity of the G peak, top image, is roughly at its most intense where the $2D$ peak, middle image, is not, and vice versa. This is not a surprising result, as graphene itself has a pronounced $2D$ peak, and as the graphene becomes more graphitic in nature, the $2D$ peak becomes suppressed and the G peak becomes more prominent. Because the ratio of the $2D$ to the G peak is often used as a metric for determining the number of graphene layers, the image of this ratio is shown as

well, at the bottom of the column. For the first set of images, this ratio image corresponds almost exactly to the $2D$ peak image, which shouldn't come as any surprise.

The right column shows the same set of images (from top to bottom, G peak, $2D$ peak, and $2D/G$ ratio) from a different area of the sample. Although the contrast inversion between the G peak image and the $2D$ peak image is not as apparent as it was in the first series of images, the $2D/G$ ratio image shows clear areas where the sample is more graphitic or graphenic. These results are exactly what we would expect for undoped graphene, and they provide a reasonable baseline for comparison in future experiments with doped graphene and more precise measurements.

After demonstrating the system's capabilities in imaging and differentiating regions of graphene and graphite, position correlation was added to the experiment to further analyze samples of this nature. In Figure 4.5, the raw optical image is shown, where there appears to be large areas of graphene with some tears in the surface that should be bare ITO, and some large wrinkles near these tears which are expected to show more graphitic features. Examination of the AFM image in Figure 4.5 seems to confirm this hypothesis, as there is a large area at roughly a certain height, with a wrinkle that is much higher and a small region near the wrinkle, which should be the tear, at a slightly lower height. The confocal image on the very right is centered on the black square shown on the optical and AFM images and shows that the wrinkle appears to be slightly more reflective than the rest of the surface. This image is a smaller scan centered at the black square in the previous two images taken mainly to aid in Raman alignment.

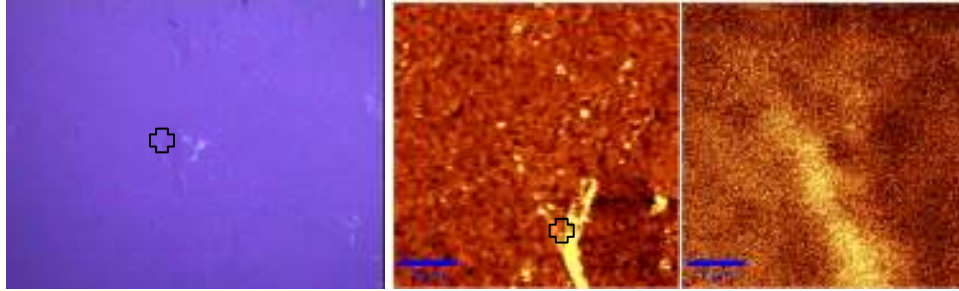


Figure 4.5: Optical (left) and 10x10 μm AFM (middle) of a selected region of an undoped graphene sample and a 5x5 μm confocal microscopy (right) centered on the cross overlayed on the AFM image

Raman images of the area centered about the black square in the optical and AFM images of Figure 4.5, and corresponding closely to the confocal image shown in Figure 4.5, are shown in Figure 4.6. Unsurprisingly, the *D* peak image, the upper left image of the figure, shows a larger concentration of defects along the wrinkle near the bare area. The *G* peak, upper right, image indicates that this wrinkle is more multilayer in nature than its surroundings. Although the raw *2D* peak intensity, seen in the lower left image of Figure 4.6, is greater along the wrinkle as well, the individual spectra extracted from the points labeled with shapes will show that this region has more layers than the surrounding parts of the sample.

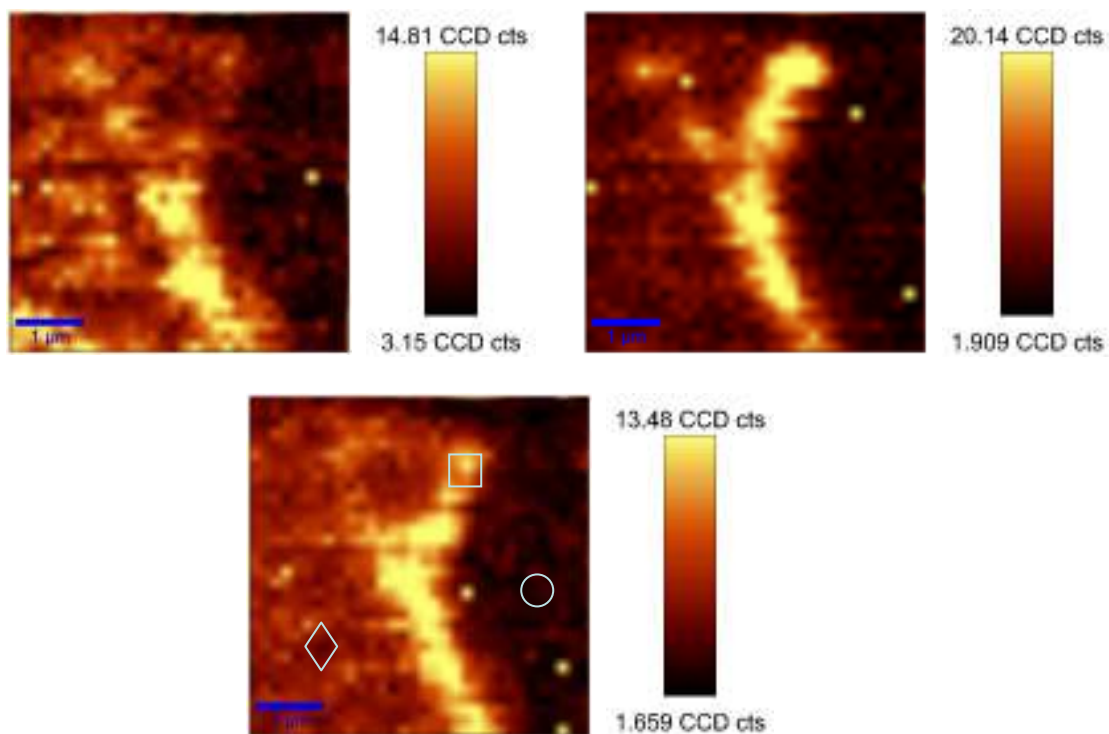


Figure 4.6: *D* peak (upper left), *G* peak (upper right), and *2D* peak (bottom) Raman images, diamond, square, and circle denote locations where individual spectra were extracted and analyzed.

At the symbols marked in Figure 4.6, individual spectra were extracted for further analysis. These spectra are shown in Figure 4.7. From the square, which is right along the wrinkle, we see that the *D* and *G* peaks are quite pronounced while the *2D* peak is extremely weak. This appears to confirm that the region of the wrinkle is more graphitic and has more defects than the rest of the sample. From the diamond, we see that the *2D* peak, while weak, is still noticeably larger than the *G* peak. Given that the detector's sensitivity in the region of the *2D* peak is weaker than elsewhere, this seems to be a good indication that this area is more like graphene in nature. From the circle, which corresponds roughly to a bare area in the optical and AFM images, we see nothing except for the slight shoulder at around 400 rel. 1/cm, which is a small fluorescence shoulder from the ITO substrate and not from any of the graphene samples themselves. These

spectra confirm that Raman imaging can provide the information needed to determine the local quality and number of layers of graphene samples and show that ITO, while it exhibits a small fluorescence signal, does not have enough fluorescence to overwhelm the Raman signal from graphene.

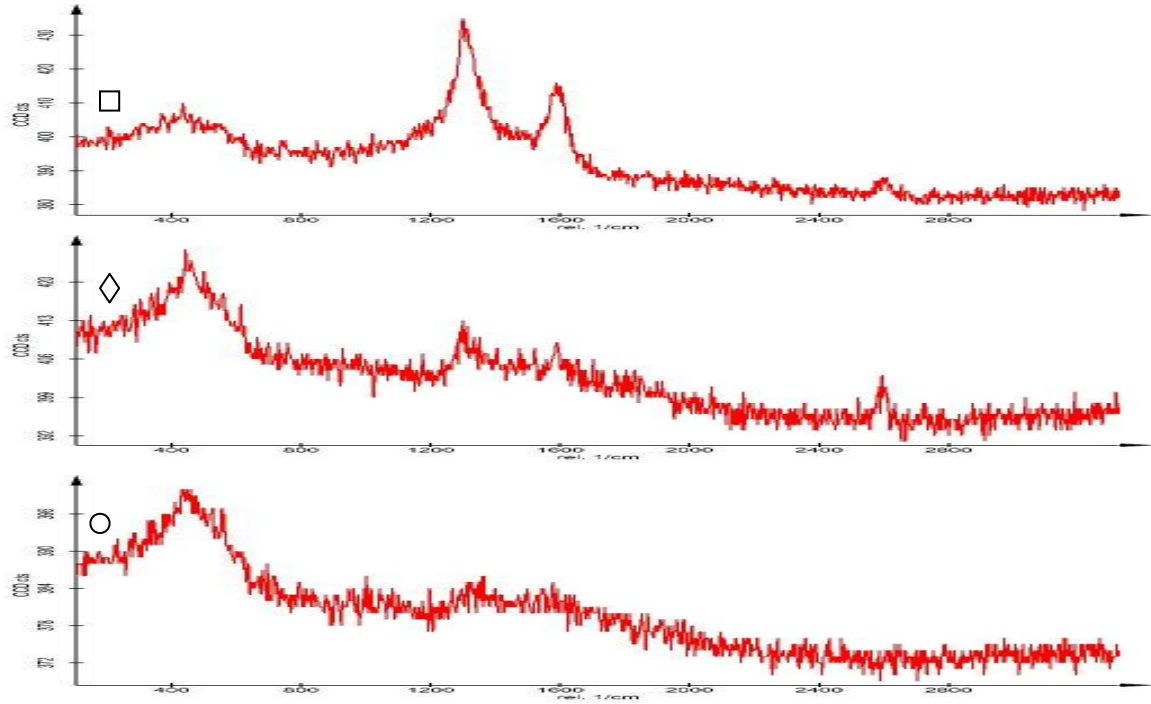


Figure 4.7: Spectra from the labeled locations in Figure 4.6

While the utility of Raman imaging for graphene is clear, the more interesting question is how to obtain dopant information from Raman spectra and images of Raman spectra. Shown in Figure 4.8 are typical graphene spectra obtained from our graphene on ITO samples. The *G* peak occurs at 1591 rel. 1/cm, which is a slightly higher shift than reported in the literature for undoped graphene, which indicates that the ITO substrate

dopes the graphene to some extent. Of note in this figure is that the *G* peak is fairly sharp, with no obvious extraneous features.

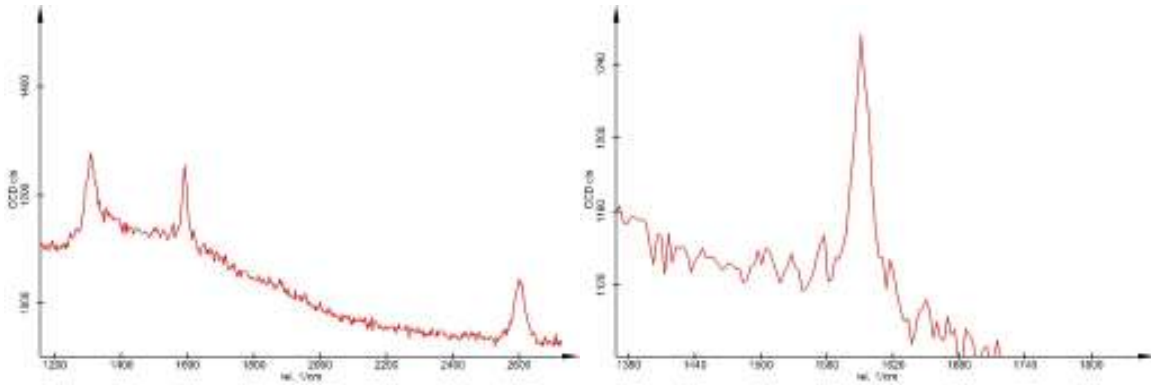


Figure 4.8: Typical spectrum of undoped graphene on ITO

As seen in Figure 4.9, on the other hand, the *G* peak for nitrogen doped graphene exhibits a small shoulder just to the right of the main *G* peak, which matches what is expected from the literature [55, 56]. The *G* peak also shifts in location slightly as well with increased doping, and for most of these spectra lies at about 1584 rel. 1/cm. The *G* peak shift and the shoulder resulting from the nitrogen doping provide excellent opportunities to utilize Raman imaging to determine the amount of doping in a particular sample of doped graphene.

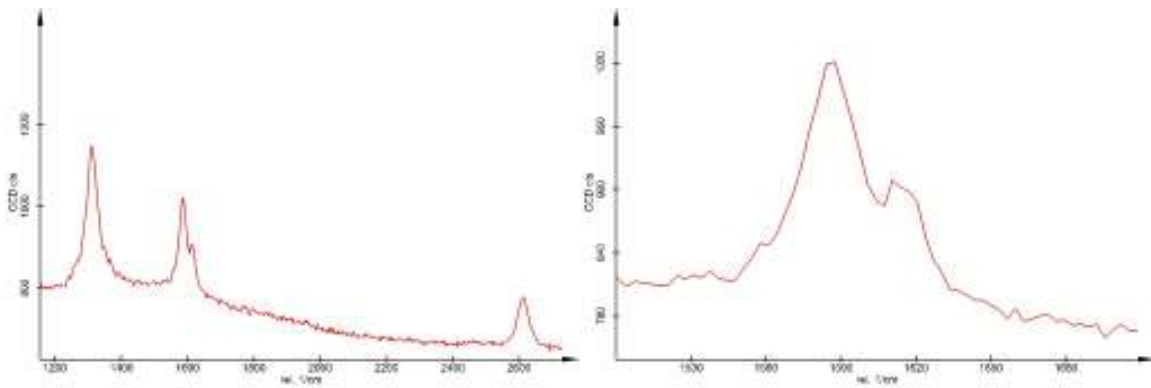


Figure 4.9: Typical spectrum of N-doped graphene on ITO

Toward this end, a high resolution image of an N-doped graphene on ITO sample was taken, the results of which are shown in Figure 4.10. This series of images was taken with a 30 s integration time to allow for a more detailed analysis of the sample in question.

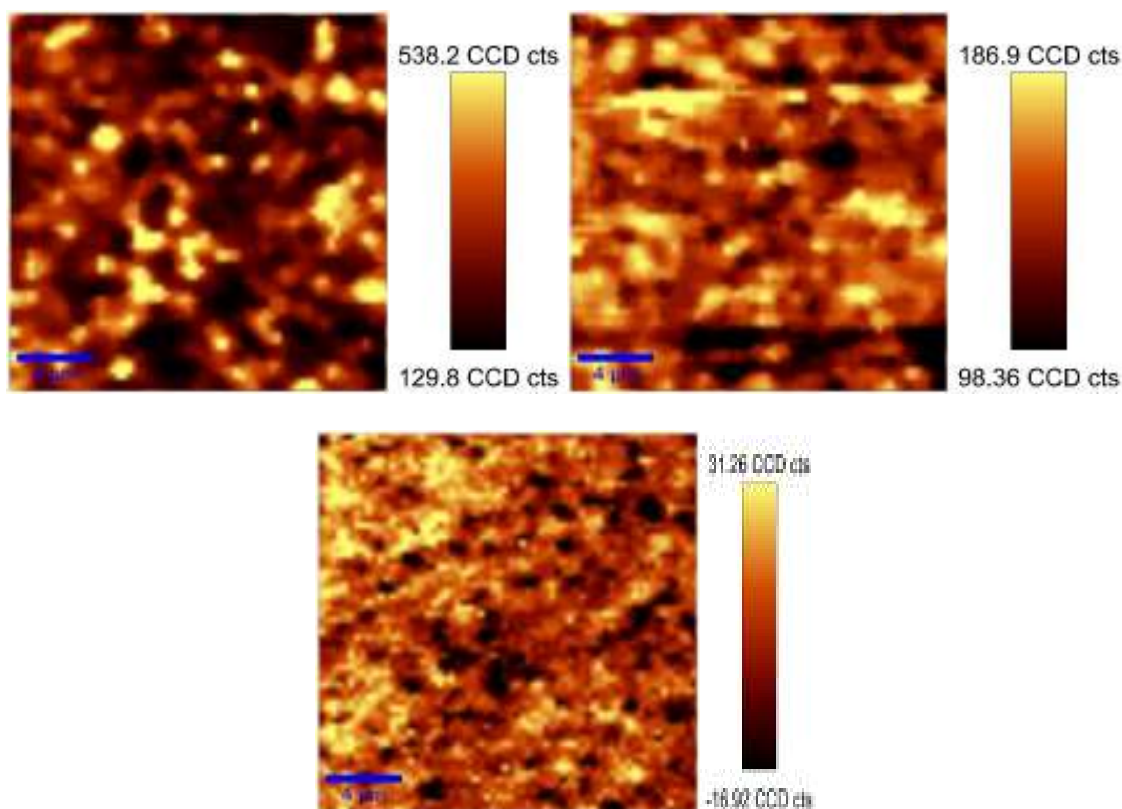


Figure 4.10: *G* peak (left), *2D* peak (right) and “N” peak images (bottom) of an N-doped graphene sample

Of particular interest is the “N” shoulder image at the very right of Figure 4.10. This image seems to show regions of higher nitrogen presence in some areas than others. Unfortunately, without a solid correlation between nitrogen shoulder size and dopant concentration, exact dopant levels are difficult to extract, however, Raman imaging can be used to show differences in dopant concentration and potentially be used for determining dopant levels in doped graphene substrates.

Another feature that changes with dopant concentration is the location of the *G* peak. This image is shown in Figure 4.11. Although somewhat rough, there is a correlation between the “N” peak image and the *G* peak shift image. The *G* peak shifts more in the top left corner and toward the left side of the image, which roughly lines up

with the high intensity areas of the “N” peak image. Conversely, toward the middle and bottom right of the image, the *G* peak shifts less, roughly correlating with the lower intensity regions of the “N” peak image. The resolution of this grating is probably interfering with our ability to make a more quantitative comparison, since each pixel covers 3 μm .

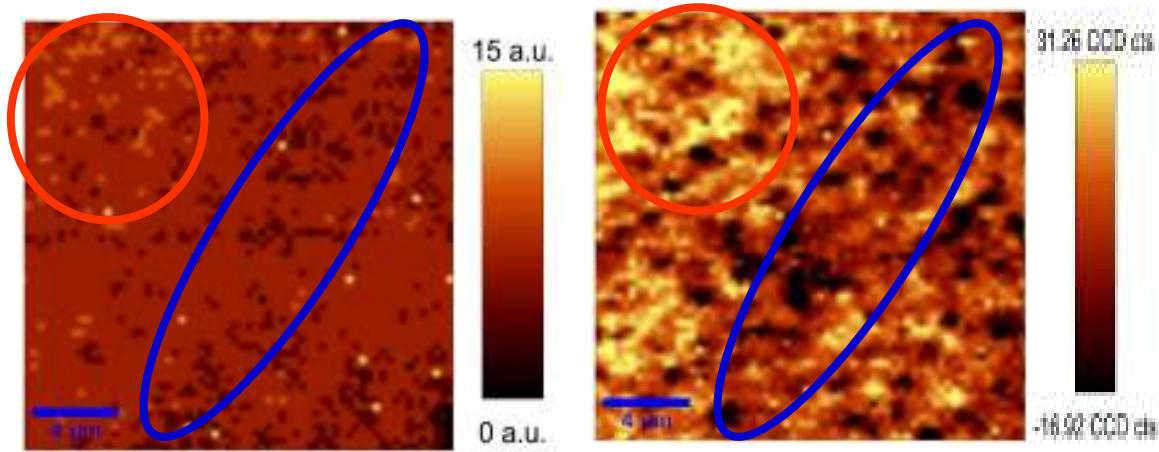


Figure 4.11: *G* peak shift from 1591 rel. 1/cm (left) and “N” peak image (right). Red circle denotes area of high nitrogen concentration while the blue circle denotes an area of lower concentration.

While a more quantitative analysis of the local dopant concentration in doped graphene is ideal, until more calibration experiments are performed on well characterized and homogenous samples of nitrogen doped graphene, this remains extremely difficult. From this set of experiments, however, the local dopant density should be extractable from Raman imaging data.

4.8 Discussion and Conclusions

The capabilities of Raman imaging for use in analyzing graphene and doped graphene samples are readily demonstrated. In undoped graphene samples,

differentiating between areas that are more like graphene and areas that are more like graphite is relatively clear, even with this detector's suppressed sensitivity to the $2D$ peak when a 785 nm laser is used. Correlation with AFM and optical images provides further reinforcement of the characteristics of the areas in question.

While analysis of nitrogen doped samples is more difficult because of the dopants suppression of the $2D$ peak, a great deal of information can still be extracted from Raman imaging of doped graphene. Although determining the number of layers is extremely tricky, because of the aforementioned $2D$ peak suppression and the change in the shape of the G peak with increased doping, important information such as the dopant concentration can still be extracted. By examining both the shift of the G peak and correlating this information with the size of the "N" peak, qualitative regions of higher and lower doping are observed. Some efforts have been made to quantify the relationship between the G peak shift and dopant concentration [54], a rigorous study has yet to be performed. Between our spectrometer's resolution of 3 $1/\text{cm}$. and the lack of a strong study relating G peak shift and dopant concentration, drawing a conclusion stronger than what has already been stated is premature.

Although a quantitative analysis was not performed, with better characterization of the impact of doping on the G peak shift and height of the "N" peak, there is no reason this technique cannot be applied to determining local dopant levels in graphene. Raman imaging has proven to be a power tool for analyzing graphene samples in the past and should prove to be a useful technique for the analysis of and profiling of doped graphene in the future.

Chapter 5

Conclusions and Future Work

5.1 Nanoparticles over Thin Film

Raman signal enhancement from a spherical nanoparticle over a thin gold film is clearly demonstrated. Because of the frequency of the incident laser, and the correlated AFM and SEM images, the enhancement can only arise from the plasmon coupling of the gold nanoparticle over the gold film. While this enhancement is present for multiple configurations, the importance of the choice of film thickness and nanoparticle size and shape is apparent.

Because of the dependence on nanoparticle size, nanoparticle shape, and metal film thickness, this system demonstrates some degree of tunability. For the series of experiments covered in this document, the 80 nm spherical nanoparticle coupled with a 20 nm thin gold film produced the best results. Other sizes of nanoparticles were tested along with different film thicknesses, and in one instance a more cylindrical nanoparticle was also examined, all of which produced a noticeably smaller signal than the optimal configuration noted above.

While near-field scanning optical microscopy (NSOM) is a powerful nanoscale technique for obtaining chemical information, the application of the above mentioned research to fabricating plasmonically enhanced NSOM probes would enhance the power of NSOM. Raman spectroscopy with scanning probe resolution has typically proven difficult because of the low light intensity involved with traditional NSOM setups. NSOM probes that have been engineered to take advantage of plasmonic enhancements,

and substrates that could couple with these probes for additional enhancement, would solve the weak signal issue and contribute toward expanding the capabilities for NSOM.

For immediate future work on experiments more directly related to what has been studied, the largest improvement would be seen in implementing a side illumination setup. The component of the electric field oriented in the desired direction resulting from a perpendicular illumination of the particle and substrate is too weak for extensive quantitative analysis. Transitioning to a laser incident at an angle would greatly increase the component of the electric field in the desired direction, which would improve signal strength and enable a more thorough analysis of the nanoparticle over thin film system.

Another avenue of interesting immediate future work would be the incorporation of other metals. While gold is a commonly used metal for plasmonic applications, because the plasmonic peak resulting from the nanoparticle-thin film coupling lies at a different location than that of the native bulk and native nanoparticle plasmons, other metals typically overlooked for SERS applications become attractive. Of particular note is aluminum, which is not commonly used for such applications because of its plasmon lying too far in the blue region, becomes particularly attractive.

Alternate particle geometries also provide another avenue of future research. The main problem for different shapes would be ensuring proper orientation relative to the surface, since the desired part of the nanoparticle must be near the thin film. If the positioning issue can be resolved, particles such as nanopyramids or other particles with a sharper shape become more attractive alternatives, since the enhancement should be much larger than a spherical nanoparticle when coupled to a film, provided the proper excitation source is used.

While the work presented in Chapter 3 goes a long way toward showing the viability and tunability of the nanoparticle over film system for plasmonic enhancement applications, there remain a large number of potential research avenues that warrant further study for the purpose of expanding the capabilities of nanoscale chemical imaging.

5.2 Work Function of Nanoparticles in STM

STM, and dI/dZ imaging in particular, has been performed on Au, Pd, and AuPd nanoparticles. By looking at the work function values of the three particles, relative to the background substrate, the difference in structure between the three particles becomes clear. The particle of interest, the AuPd particle, shows a relative work function value that is quite close to the Pd particle, with a small increase that may be caused by some of the inner gold core being exposed.

The most likely cause of this small discrepancy between the Pd and AuPd values is that part of the gold core is exposed. Because the MATLAB program used to analyze the dI/dZ images averages a small 3 x 3 pixel area to try to prevent small fluctuations from dominating the extracted value, small areas of exposed gold would cause a higher relative work function value to be averaged in with the rest of the extracted values. Because the gold cores are coated with palladium, the other extracted values should have a relative work function identical to the values seen on Pd nanoparticles.

While a more rigorous quantitative analysis would be preferable, the immobilization strategy employed poses somewhat of a barrier. Because both the substrate and the nanoparticle are coated by a SAM, the STM is not directly measuring the dI/dZ value of the substrate/nanoparticle. The differences in work function value are

a result of different strengths of interaction between the gold substrate and the various nanoparticles, so it is quite likely that the difference between the work function of the nanoparticle and the work function of the gold substrate is somewhat muted because the work function measurements in this document are, in a sense, indirect.

For this reason, future experiments should attempt a different strategy to immobilize the particles. In addition to the measurement difficulties mentioned above, the AuPd particles are still quite mobile even with utilizing SAM entanglement to hold them in place. A general adhesive layer, like poly-4-vinylpyridine, may be useful in this case. There may be some concern that the polymer layer would be too thick to allow for tunneling between the STM tip and the gold substrate. If this concern is unwarranted, however, the fact that nanoparticles would remain immobilized on the surface without the need to coat the entire particle in the molecular layer would provide a method for direct probing of the nanoparticle's work function.

Another factor that may aid in future experiments would be implementing a method to clean the STM tip in the ultra-high vacuum chamber. STM run in its default configuration is already somewhat sensitive to impurities on the tip, and this sensitivity is magnified for a technique as tricky as dI/dZ imaging. Electron bombardment, where the tip is exposed to energized electrons in order to remove anything from the apex of the tip, would work nicely. Tip cleaning in combination with using a less reactive tip, perhaps Ti instead of Pt/Ir, would go far in allowing for a more rigorous quantitative analysis of these particles.

Although there are many gaps which can be filled with the above suggestions for future direction, the differences in work function between Au, Pd, and AuPd nanoparticles has been shown using dI/dZ imaging in an STM.

5.3 Raman Spectroscopy of Graphene

Raman spectroscopy was performed on graphene, both pristine and doped. Distinct differences between the spectra should make it possible to determine areas that contain dopants and areas that are dopant free on a particular sample of graphene. Through Raman imaging, the rough number of layers, by looking at the *2D* and *G* peaks, and the general quality, from the *D* peak, of a graphene segment can be determined at a submicron level. The qualitative dopant levels from a sample of nitrogen doped graphene were also determined.

That Raman spectroscopy can be used to determine and map relative dopant concentrations has been shown. Through examining both the dopant induced shoulder by the *G* peak as well as the shift of the *G* peak, Raman spectroscopy was used to generate an image of the dopant concentration of a doped sample of graphene. Although these results show how powerful Raman spectroscopy can be in analyzing the dopant profiles of doped graphene, further measures can be taken to obtain a more quantitative, and thus more practically useful, measurement.

Exploration in conjunction with careful optical measurements could provide a more quantitative measure of dopant concentration. Absorption measurements have been used to determine the number of layers present. Because both doping and multiple layers cause a decrease in a *2D* peak of graphene, Raman alone is most likely insufficient to

differentiate between multiple layers and increased dopants. In the future, careful calibration may allow for examining the *G* peak shift or the dopant shoulder, and comparing the size of these values with the expected *2D* peak reduction, however, without an initial baseline obtained from carefully constructed single layer and known multiple layer doped graphene samples, rigid quantitative analysis utilizing only Raman spectroscopy becomes difficult at best.

In that sense, generating a database of baseline Raman spectra using optical measurements to determine number of layers and perhaps x-ray photoelectron spectroscopy (XPS) to determine the dopant concentration would be ideal. If all of these measurements were correlated with each other, a table of Raman spectra dependent upon number of layers and dopant concentration could be obtained. Unfortunately, the fact that other defects would lead to a further reduction of the *2D* peak would complicate matters.

Another change that would help with this experiment in particular is a different laser source. All of the experiments were carried out using a 785 nm laser, however, at this excitation wavelength, the *2D* peak ends up occurring well into the reduced sensitivity regime of silicon detectors. Another option would be to switch detectors to one more sensitive a bit further into the infrared, however, these detectors can be cost prohibitive to implement and laser sources more to the blue end of the spectrum can be more easily obtained.

To aid in the analysis of *G* peak shifts, a finer grating would make more precise analysis possible. The grating chosen for this series of experiments is limited to 3 1/cm. per CCD array pixel, so *G* peak shifts smaller than 3 1/cm. are not detected as a shift. A

finer grating would increase this resolution, allowing for a more rigorous analysis of G peak shift versus dopant concentration. Because of the detector sensitivity issue mentioned above, merely swapping in a finer grating was not a feasible option for this series of experiments, but a finer grating in conjunction with a different laser source would provide more leeway for analysis.

Even within these limitations, Raman spectroscopy of graphene and doped graphene is a useful method for the investigation of graphene quality and dopant profiles. Further refinements in the future could bring things up to a potentially industrially viable analysis tool.

References

- [1] Demtroder, W., *Laser Spectroscopy*, (Springer, 1998).
- [2] Lyon, L.A., et. al., *Analytical Chemistry* **70**, 341R-361R (1998).
- [3] Schatz, G.C., et. al., in *Topics in Applied Physics; Vol. 103: Surface Enhanced Raman Scattering Physics and Applications*, Kneipp, K., Moskovits M., Kneipp, H. eds., (Springer), New York, 2006, pp.19-46.
- [4] Hartschuh, A., et. al., *Physical Review Letters* **90**, 095503 (2003).
- [5] Hartschuh, A., et. al., *Science* **301**, 1354-1356 (2003).
- [6] Bohren, C.F. and Huffman, D.R., *Absorption and Scattering of Light by Small Particles*, (Wiley-Interscience, 1998).
- [7] Scaffardi, L.B., et. al., *Nanotechnology* **16**, 158-163 (2005).
- [8] Link, S., et. al., *Journal of Physical Chemistry B* **103**, 3073-3077 (1999).
- [9] Liao, H. and Hafner, J.H., *Journal of Physical Chemistry B* **108**, 19276-19280 (2004).
- [10] Liao, H. and Hafner, J.H., *Chemistry of Materials* **17**, 4636-4641 (2005).
- [11] Averitt, R.D., et. al., *Physical Review B* **58**, R10203-R10206 (1998).
- [12] Oldenburg, S.J., et. al., *Journal of Chemical Physics* **111**, 4729-4735 (1999).
- [13] Oldenburg, S.J., et. al., *Chemical Physics Letters* **288**, 243-247 (1998).
- [14] Hill, W. and Wehling, B., *Journal of Physical Chemistry* **97**, 9451-9455 (1993).
- [15] Bryant, M.A. and Pemberton, J.E., *Journal of the American Chemical Society* **113**, 8284-8293 (1991).
- [16] Roth, P.G. and Boerio, F. J., *Journal of Polymer Science: Part B: Polymer Physics* **25**, 1923-1933 (1987).
- [17] Zeisel, D., et. al., *Chemical Physics Letters* **283**, 381-385 (1998).
- [18] Grabar, K.C., et. al., *Analytical Chemistry* **67**, 735-743 (1995).
- [19] Zhou, Q., et. al., *Journal of Physical Chemistry B* **110**, 12029-12033 (2006).

- [20] Freeman, R.G., et. al., *Science* **267**, 1629-1632 (1995).
- [21] Haes, A.J., et. al., *Journal of the American Chemical Society* **128**, 10905-10914 (2006).
- [22] Zhang, X., et. al., *Vibrational Spectroscopy* **42**, 2-8 (2006).
- [23] Mahajan, S., et. al., *Physical Chemistry Chemical Physics* **9**, 104-109 (2007).
- [24] Jackson, J.B. and Halas, N.J., *Proceedings of the National Academy of Sciences* **101**, 17930-17935 (2004).
- [25] Levin, C.S., et. al., *Analytical Chemistry* **78**, 3277-3281 (2006).
- [26] Levin, C.S., et. al., *Nano Letters* **6**, 2617-2621 (2006).
- [27] Le, F., et. al., *Nano Letters* **5**, 2009-2013 (2005).
- [28] Nordlander, P. and Le, F., *Applied Physics B* **84**, 35-41 (2006).
- [29] Yoon, J.K., et. al., *Journal of Physical Chemistry C* **113**, 1769-1774 (2009).
- [30] Mock, J.J., et. al., *Nano Letters* **8**, 2245-2252 (2008).
- [31] Sick, B., et. al., *Physical Review Letters* **85**, 4482-4485 (2000).
- [32] Malynych, S., et. al., *Journal of Physical Chemistry B* **106**, 1280-1285 (2002).
- [33] Wiesendanger, R., *Scanning Probe Microscopy and Spectroscopy: Methods and Applications*, (Cambridge University Press, 1994).
- [34] Chen, C. J., *Introduction to Scanning Tunneling Microscopy*, (Oxford University Press, 1993).
- [35] Hasegawa, Y., et. al., in *Advances in Scanning Probe Microscopy*, Sakurai, T. and Watanabe, Y. eds. (Springer-Verlag), Berlin, 2000, pp. 167-191.
- [36] Sakai, A., in *Advances in Scanning Probe Microscopy*, Sakurai, T. and Watanabe, Y. eds. (Springer-Verlag), Berlin, 2000, pp. 143-165.
- [37] Smith, R.K., et. al., *Progress in Surface Science* **75**, 1-68 (2004).
- [38] Poirier, G.E., et. al., *Langmuir* **17**, 1176-1183 (2001).
- [39] Donnhäuser, Z.J., et. al., *Science* **292**, 2303-2307 (2001).

- [40] Donnhauser, Z.J., et. al., *Japanese Journal of Applied Physics* **41**, 4871-4877 (2002).
- [41] Cygan, M.T., et. al., *Journal of the American Chemical Society* **120**, 2721-2732 (1998).
- [42] Anderson, M.E., et. al., *Journal of Vacuum Science and Technology B* **21**, 3116-3119 (2003).
- [43] Evans, S.D., et. al., *Journal of the American Chemical Society* **113**, 5866-5868, (1991).
- [44] Hatzor, A. and Weiss, P.S., *Science* **291**, 1019-1020, (2001).
- [45] Heck, K.N., et. al., *Journal of Catalysis* **267**, 97-104, (2009).
- [46] Fang, Y.L., et. al., *ACS Catalysis* **1**, 128-138, (2011).
- [47] Fang, Y.L., et. al., *Catalysis Today* **160**, 96-102, (2011).
- [48] Nutt, M.O., et. al., *Applied Catalysis B: Environmental* **69**, 115-125, (2006).
- [49] *CRC Handbook of Chemistry and Physics*, Weast, R.C. and Astle, M.J., eds. (CRC Press, Inc.), Boca Raton, 1980, p. E83.
- [50] Alloway, D.M., et. al., *Journal of Physical Chemistry B* **107**, 11690-11699, (2003).
- [51] de Boer, B., et. al., *Advanced Materials* **17**, 621-625, (2005).
- [52] Dresselhaus, M.S., et. al., *Nano Letters* **10**, 751-758, (2010).
- [53] Ferrari, A.C., et. al., *Physical Review Letters* **97**, 187401, (2006).
- [54] Panchakarla, L.S., et. al., *Advanced Materials* **21**, 4726-4730, (2009).
- [55] Lin, Y.C., et. al., *Applied Physics Letters* **96**, 133110, (2010).
- [56] Shao, Y., et. al., *Journal of Materials Chemistry* **20**, 7491-7496, (2010).
- [57] Reddy, A.L.M., et. al., *ACS Nano* **4**, 6337-6342, (2010).
- [58] Pimenta, M.A., et. al., *Physical Chemistry Chemical Physics* **9**, 1276-1291, (2007).
- [59] Ferrari, A.C., *Solid State Communications* **143**, 47-57, (2007).